Electromechanical Resonances in Suspended Bilayer Graphene

Matthew Storms

A Thesis

in

The Department

of

Physics

Presented in Partial Fulfillment of the Requirements

For the Degree of Master of Science

Concordia University

Montréal, Québec, Canada

September 2019

Concordia University

School of Graduate Studies

This is to certify that the thesis prepared

By: **Matthew Storms**

Entitled: **Electromechanical Resonances in Suspended Bilayer Graphene**

and submitted in partial fulfillment of the requirements for the degree of

Master of Science

complies with the regulations of this University and meets the accepted standards with respect to originality and quality.

Signed by the final examining commitee:

Dr. Valter Zazubovits _____ Chair

Dr. Pablo Bianucci _____ Examiner

Dr. Saurabh Maiti _____ Examiner

Dr. Alexandre Champagne _____ Supervisor

Approved _____

Chair of Department or Graduate Program Director

_____ 20 _____ _____

Dean of Faculty

Abstract

Electromechanical Resonances in Suspended Bilayer Graphene

Matthew Storms

Bilayer graphene is a promising material to explore the physics of two-dimensional Nanoelectromechanical Systems (NEMS) due to its mechanical strength and low-onset nonlinearity. We describe a procedure to fabricate and anneal bilayer graphene NEMS (BG-NEMS) which are nearly disorder free (charge mobility $\mu \approx 76000\, cm^2/Vs$, charge doping $n_0 < 6.6 \times 10^{-9}\, cm^{-2}$, mass density $\rho \approx 1.01\, \rho_{graphene}$).

We calibrate a current mixing measurement circuit for simultaneous resonance actuation, resonance detection, and conductivity measurement in annealed BG-NEMS. Using our circuit, we detect high-quality and reproducible BG-NEMS resonances with frequencies in the range $f_0 = 137\, MHz$ to $f_0 = 220\, MHz$ and quality factors of $Q > 3000$ at amplitudes between $\delta z = 50\, pm$ and $\delta z = 1\, nm$.

Our data show significant Duffing nonlinearity ($\alpha \approx -1.0 \times 10^{35}\, Hz^2/m^2$). When the resonators are strained, we observe anomalous frequency tuning. At higher powers our data show mode mixing with high cooperativity ($C \approx 4$ and $C \approx 36$). The mode mixing ($\alpha_{12} \approx 6.9 \times 10^{33}\, Hz^2/m^2$ and $\alpha_{12} = 3.3 \times 10^{36}\, Hz^2/m^2$) matches the Duffing parameter and suppresses mobility (low μ) and electromechanical dissipation (high Q).

Disordered morphology of the samples accounts for decreased mobility (lattice disorder associated with ripples and wrinkles), mode mixing (nonlinear mode coupling to ripples), and anomalous membrane dispersion (catenary wrinkle deformation).

Acknowledgments

I could not have completed this project without substantial help along the way; a full list of acknowledgments would not be possible. I have nonetheless tried to include the most immediate and relevant mentions below.

Firstly, I want to thank my supervisor and mentor Dr. Alexandre Champagne for his helpful discussions, intuition, enthusiasm, and support during my MSc project. My thanks also go to my other thesis committee members—Dr. Laszlo Kalman and Dr. Pablo Bianucci—for their helpful comments on my progress reports and my research seminar. I also thank Dr. Saurabh Maiti for volunteering his time as a replacement committee member for the defence.

Next, I want to recognize the importance of training and advice I received from Dr. Marc Collette and Dr. Andrew McRae in the operation of instruments and software required for the completion of my project. Thank you both for sharing your time and experience with me.

I would also like to acknowledge the support I received from the Concordia University Faculty of Arts and Science Graduate Fellowship, the Richard K. Dimond Memorial Award, and the Mostafa Showleh Physics Teaching Assistant Award.

On a personal note, I thank my mother and father—Kathleen Cornish and Reginald Storms—for their love and support as well as for being scientific role-models since the time I was young. Finally, my thanks to all the members of the Champagne Group for their friendship in the lab.

Contents

List of Figures

List of Tables

List of Acryonyms

2D Two-Dimensional

3D Three-Dimensional

AC Alternating Current

AFM Atomic Force Microscopy

AM Amplitude Modulation

BG-NEMS Bilayer Graphene Nanoelectromechanical System

CNP Charge Neutrality Point

DC Direct Current

EMR Electromechanical Resonance

FM Frequency Modulation

FQHE Fractional Quantum Hall Effect

HOPG Highly-Ordered Pyrolitic Graphite

MEMS Microelectromechanical System

MMA Methyl Methacrylate

NEMS Nanoelectromechanical System

PMMA Polymethyl Methacrylate

RF Radio Frequency

SEM Scanning Electron Microscope

List of Variables

α_2 quadratic nonlinearity of an oscillator

α_3 cubic (Duffing) nonlinearity of an oscillator

α_{ij} nonlinear mode coupling of an oscillator

c_G gate capacitance per unit area

Δ_ω size of the frequency gap at an avoided crossing

δz mechanical amplitude of a NEMS oscillator

E 3D elastic (Young's) modulus

e elementary unit of charge

ε uniaxial mechanical strain in a material

η nonlinear damping of an oscillator

F driving force of an oscillator

f resonance frequency of an oscillator

G conductance of a transistor

γ linear damping of an oscillator

h height of graphene channel suspended above the gate

I DC current

I^{mix} mixing current

k spring constant of an oscillator

L length of the suspended portion of a doubly-clamped NEMS

m mass of a resonator

μ_e mobility for electrons

μ_h mobility for holes

n planar charge density

ω angular frequency

ϵ relative permittivity of a material

ϕ phase offset between the RF gate and source signals at the sample

Q quality factor of a resonance

R_c contact resistance

ρ mass density of a material

σ charge conductivity of a transistor

T lattice temperature of the sample

t thickness of the gate oxide

θ phase between the resonance frequency and the drive force

V_0 gate voltage position of the charge neutrality point (also V_CNP)

V_B bias voltage

V_G gate voltage

W width of the suspended portion of a doubly-clamped NEMS

z DC vertical displacement of an oscillator from horizontal

List of Equations

Chapter 1

Carbon NEMS: Motivation to Study Bilayer Graphene NEMS

We begin this chapter with an overview of modern electromechanical systems and their applications to consumer electronics. We review recent progress in nanoelectromechanical systems (NEMS) made from one- and two-dimensional carbon allotropes like graphene, multi-layer graphene, and carbon nanotubes as the eventual evolution of electromechanical systems. We highlight the advantages of bilayer graphene relative to other NEMS in terms of its unique physics. We describe the mechanical and electronic properties of bilayer graphene, emphasizing its similarity to and differences from monolayer graphene. We conclude with an outline of this experimental thesis studying electromechanical resonances in bilayer graphene NEMS (BG-NEMS) such as the example shown in Figure 1.1.

1.1 Electromechanical Sensors for Industry and Research

Microelectromechanical Systems (MEMS) are widespread in modern consumer electronics such as clocks, barometers, thermometers, gyroscopes, hygrometers,

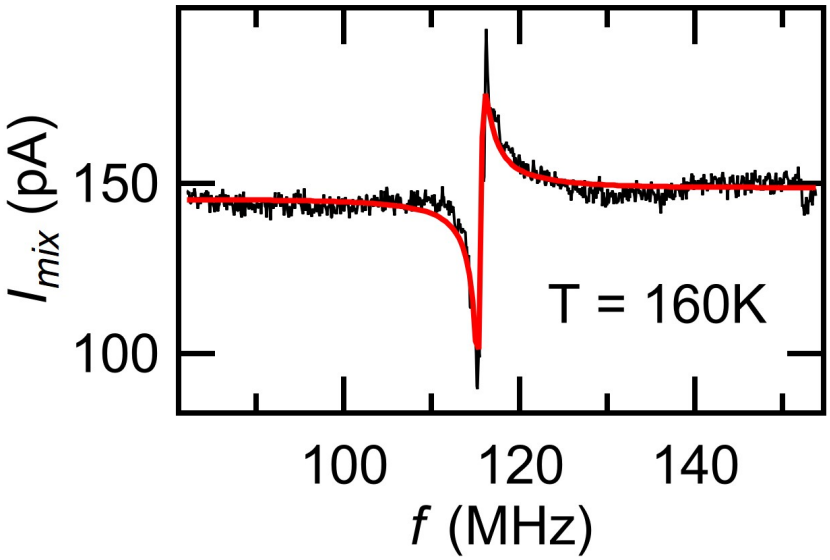

Figure 1.1: Electromechanical resonance in a bilayer graphene sample at 160K. I_{mix} (current proportional to the mechanical oscillation amplitude) versus f (a drive frequency generated by an RF source). The raw data is shown in black. A theoretical model of the resonance is presented in Chapter 3 and included here in red. From Device A.

magnetometers, and accelerometers [1]. While MEMS are traditionally many microns in size, demands for improved accuracy and energy efficiency have driven increasing miniaturization to the point where the MEMS dimensions (length and/or width/thickness) are approaching nanometer scale and below [2]. This downsizing is complicated, however, by the very small length and energy scales involved.

Nanoelectromechanical systems are the final stage in the miniaturization of the electromechanical sensors which have become ubiquitous in the last decades; NEMS sensors from 2D and 1D materials have been used as pressure sensors [3], mass sensors (as seen in Figure 1.2) with atomic resolution [4], strain sensors [5], and ultrasound detectors [6]. Because of their sensitivity, they have already been used to detect physical phenomena such as the quantum Hall effect [7], electron-phonon interaction [8], and light-matter interaction [9] at the smallest scales. Understanding physics of 2D and 1D NEMS is therefore an important technological objective.

The value of NEMS for fundamental physics research is also clear. Electronic

transport in 2D and 1D materials like graphene and carbon nanotubes is confined to a reduced number of dimensions, resulting in unusual physical properties [10]. Electromechanical oscillators made from these novel materials are a promising avenue to explore their electronics [11].

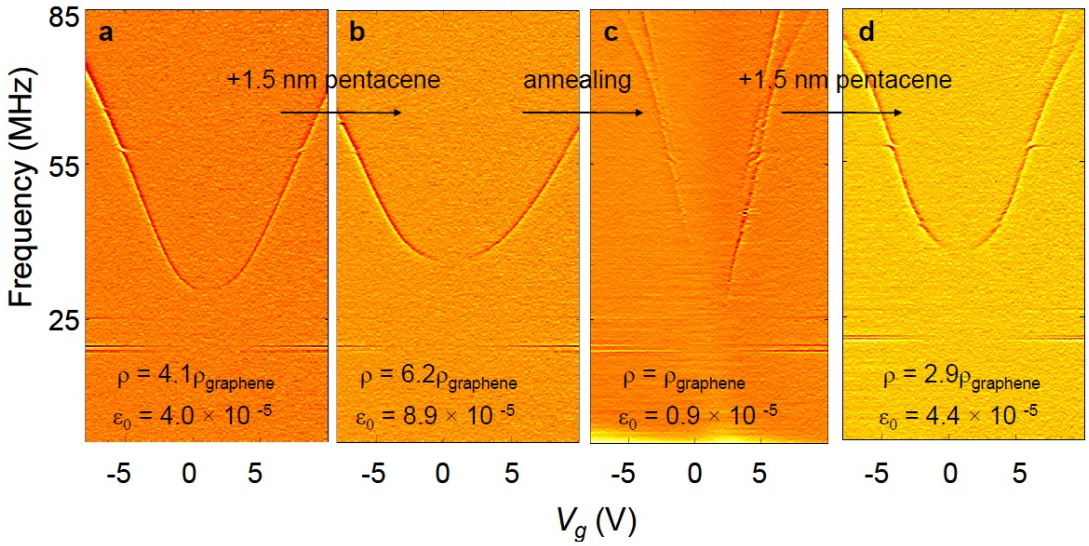

Figure 1.2: Graphene NEMS mass sensor.
Frequency ($2\pi f = \sqrt{\frac{k}{m}}$, where k describes the strain and m describes the mass) vs V_G (a gate voltage to control strain). **a** the frequency change due to increasing strain. **b** after depositing 1.5 nm of pentacene, the frequency is less tunable. **c** the tuning improves after the device is cleaned. **d** reproducing the result from **b**. This figure was reproduced from a paper by C. Chen et al. [12].

Measurements of 2D NEMS resonance (frequency, quality factor, and amplitude) have been made using frequency modulation and amplitude modulation techniques [13][14], atomic force microscope nano-indentation [15], optical readout [16], and current mixing [14]. NEMS show nonlinear behaviour at low drive amplitudes [17], bistable (or more) mechanical states [18], nonlinear mode coupling [19] as well as tunable nonlinearities which can be varied to minimize dissipation [20].

The physics accessible through the electromechanical resonance is also very rich. The quality factor is a readout of the electromechanical loss and can be used to probe all sources of dissipation simultaneously. The energy dissipation in NEMS is sensitive to electronic phase transitions (as seen in Figure 1.3) [7], potentially allowing

mechanical detection of exotic fractional quantum Hall effect states. Lastly, NEMS present a possibility to study highly nonlinear oscillators in the quantum regime [21].

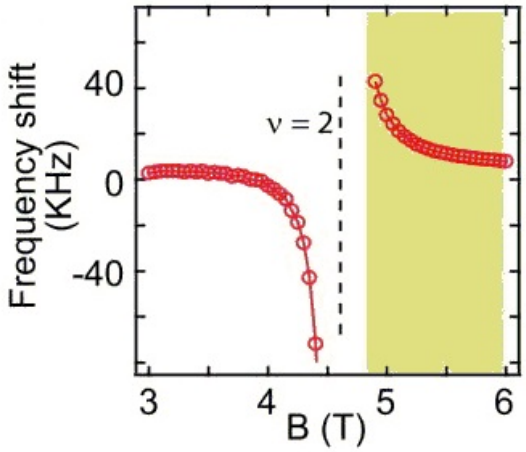

Figure 1.3: Electromechanical detection of quantum Hall effect.
The left axis is the shift in the resonance frequency; the bottom axis is the magnetic field. As the system passes through a quantum Hall phase transition, the resonance frequency is shifted by electromechanical coupling. This figure was reproduced from a paper by V. Singh et al. [7].

"2D materials" is a relatively new field of study [22] which has developed rapidly since the discovery of graphene [23]. While many 2D systems are now known, the most versatile and best studied is the original graphene. The advantages of graphene-based 2D materials are myriad: stability in air, ease of production, relative robustness, adequate simplicity for quantitatively modelling. Graphene poses several problems for applications however [10], especially in NEMS. Graphene lacks a band gap and therefore its charge conductivity cannot be "turned off" - an essential feature of logic transistors. Moreover, while some of the most interesting and potentially technologically disruptive physics takes place when there are very few charge carriers—near the so-called "Dirac Point", or "Charge Neutrality Point" (CNP). Electromechanical disorder (including wrinkles, charge density fluctuations, and impurities) often prevents robust electromechanical measurements in this regime (in the seminal paper by C. Chen et Al. [12], there was a $\sim 1\ V$ (corresponding to $\sim 1 \times 10^{10}\ cm^{-2}$) region around the CNP where the resonance could not be

distinguished from noise). Lastly, monolayer graphene is a poor platform to study the general properties of NEMS because it cannot mimic 2D heterostructures (wherein 2D materials are stacked onto one another). Bilayer graphene is a promising avenue towards overcoming all of these challenges.

1.2 The Advantages of Bilayer Graphene for Electromechanical Resonators

Bilayer graphene NEMS (BG-NEMS) are the simplest platform which can overcome many of the limitations of monolayer graphene NEMS. In bilayer graphene, it is possible to open a tunable band gap (>250 meV [24] as compared to 1.1 eV in silicon [25]) using an electric field transverse to the layers [26]. Moreover, bilayer graphene is much less sensitive to electromechanical disorder and noise at the charge neutrality point because of its parabolic (discussion in Section 1.3.2) dispersion relation [27], which leads to a non-vanishing density of states for charge carriers at low energy; specifically, this means that adding charge carriers or electromechanical fields leads to much smaller local fluctuations of the local Fermi energy than in monolayer graphene.

Whereas pristine monolayer graphene has only one crystal structure, interlayer interactions in bilayer graphene provide a simple platform to understand the vast potential of engineering layered 2D systems. For example, bilayer graphene is a fascinating laboratory for new 2D physics: twisted bilayer is the simplest system which exhibits unconventional superconductivity [28][29] (see Figure 1.4), the band gap opened by a transverse electric field is electrostatically tunable [27], and the FQHE in bilayer graphene includes even denominator states which are studied as possible topologically protected qubits [30].

Based on the present understanding of the electronic and mechanical properties of bilayer graphene, BG-NEMS can provide a versatile platform to explore and exploit the still largely unexplored electromechanical interactions in bilayer graphene.

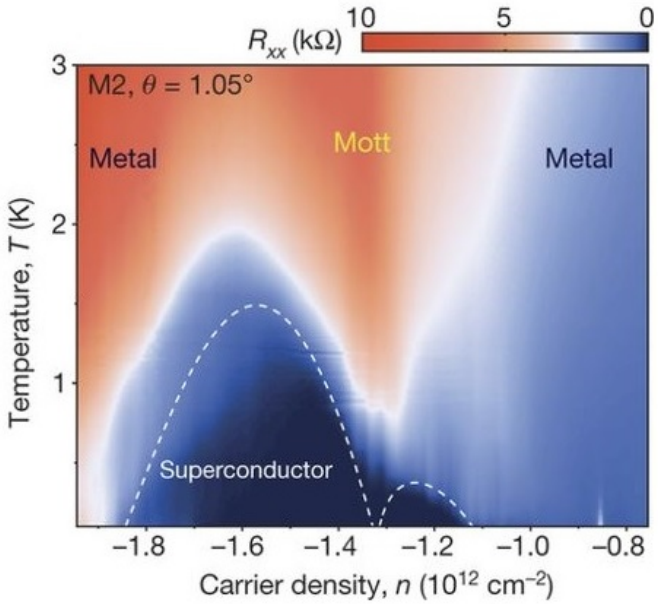

Figure 1.4: Observing unconventional superconductivity in twisted (magic-angle) bilayer graphene.
The x axis is the carrier density, the y axis is temperature, and the colour scale is resistance. A transition from an insulating state due to electron-electron interactions to a zero resistance superconducting state has been observed. This transition is characteristic of unconventional superconductors. This figure is reproduced from a paper by Y. Cao et al. [28][29]

1.3 Basics of Electronics, Mechanics, and Electromechanics in BG-NEMS

To understand the properties of BG-NEMS, it is important to be able to distinguish the excitation energies of graphene's mechanical degrees of freedom, electronic degrees of freedom, and their electromechanical couplings. To understand the mechanics and electronics of pristine bilayer graphene, we start with a discussion of its crystal structure. Using the tight-binding approximation, we then derive its electronic bands. The mechanical excitations of bilayer graphene are described by phonon modes which are also extracted from the atomic structure. In BG-NEMS, macroscopic mechanical vibrations are described as excitations of a damped harmonic oscillator.

1.3.1 Crystal Structure of Monolayer and Bilayer Graphene

The basic electronic and mechanical properties of bilayer graphene are determined by its crystal structure, which consists of stacked layers of monolayer graphene as seen in Figures 1.5 and 1.6. We begin by motivating these properties.

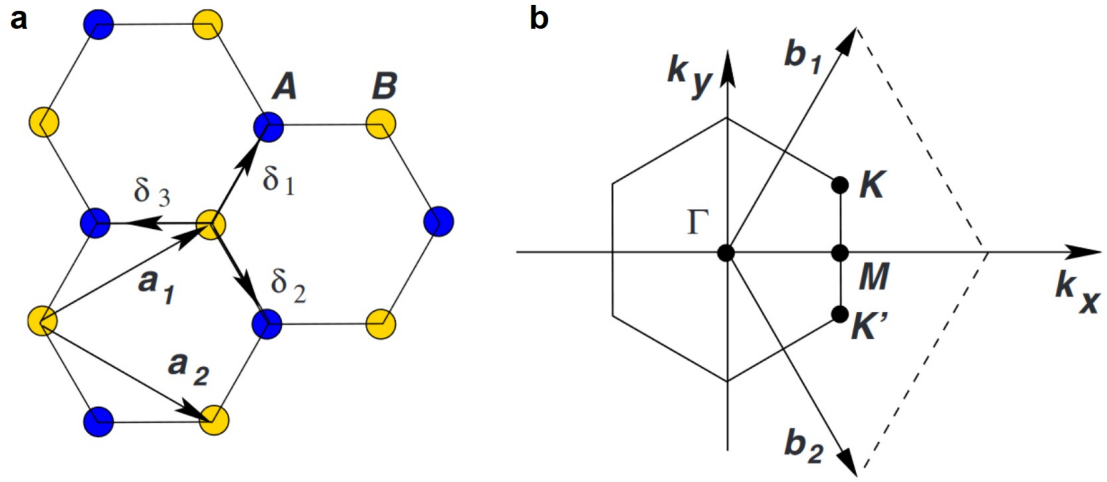

Figure 1.5: The atomic structure of monolayer graphene.
a Graphene is a honeycomb lattice (special case of hexagonal with a two atom basis). **b** The reciprocal lattice of a honeycomb is a triangular lattice with a hexagonal first Brillouin zone. This figure is reproduced from a review by A. Castro Neto et al. [10].

It is helpful to begin by familiarizing ourselves with the material in question. Graphene is a honeycomb lattice. A honeycomb lattice is a triangular lattice with lattice vectors $\vec{a}_1 = \left(\frac{3}{2}, \frac{\sqrt{3}}{2}\right) a$ and $\vec{a}_2 = \left(\frac{3}{2}, -\frac{\sqrt{3}}{2}\right) a$ where $|\delta|$ is the carbon bond length and a is the lattice constant (see figure 1.5).

The honeycomb shape is described by the basis $\vec{a} = (0, 0)$ and $\vec{b} = (1, 0)\, a$ (note that we have chosen a hexagon side length of a and oriented the armchair axis along x for definiteness). The vectors to nearest neighbours are therefore $\vec{\delta}_1 = \left(\frac{1}{2}, \frac{\sqrt{3}}{2}\right) a$, $\vec{\delta}_2 = \left(\frac{1}{2}, -\frac{\sqrt{3}}{2}\right) a$, and $\vec{\delta}_3 = (-1, 0)\, a$.

The reciprocal lattice is defined by the reciprocal lattice vectors: $\vec{g}_1 = \frac{2\pi}{3a}\left(1, \sqrt{3}\right)$ and $\vec{g}_2 = \frac{2\pi}{3a}\left(1, -\sqrt{3}\right)$. In reciprocal space, the hexagon with side length $\frac{2\pi}{3a}$ defines the first Brillouin zone. In reciprocal space, the vertices are all equivalent to one of the two points: $\vec{K} = \frac{2\pi}{3a}\left(1, \frac{1}{\sqrt{3}}\right)$ and $\vec{K}' = \frac{2\pi}{3a}\left(1, -\frac{1}{\sqrt{3}}\right)$.

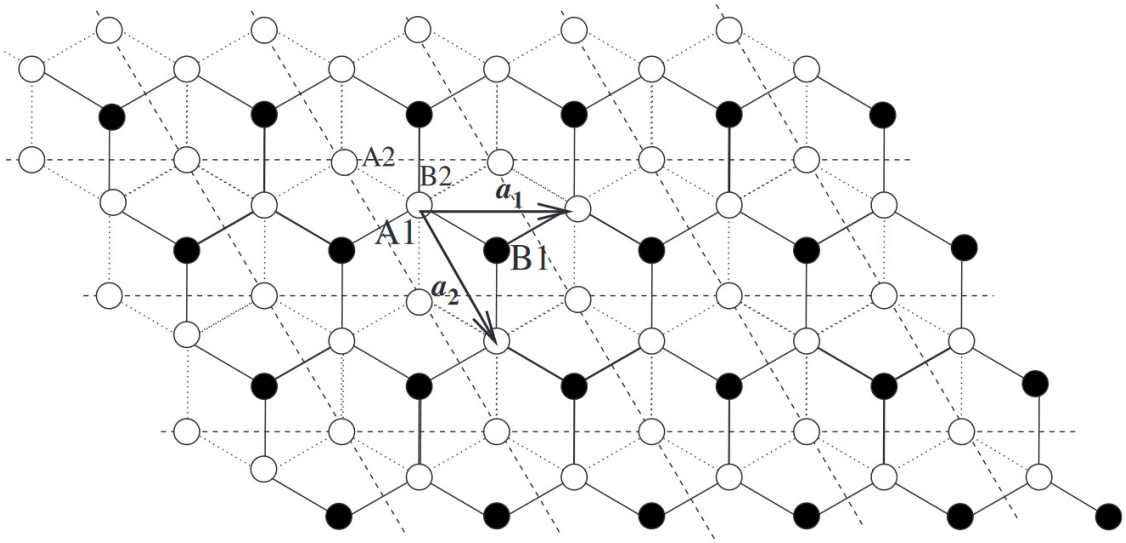

Figure 1.6: The atomic structure of bilayer graphene.
Bilayer graphene stacking is Bernal (AB). This figure is reproduced from a review by A. Castro Neto et al. [10].

We now have enough information to solve for the electronic states of monolayer graphene.

1.3.2 Electronic Structure of Monolayer and Bilayer Graphene

The electronics in graphene can be effectively described by the tight-binding model. When the dominant contribution to the Hamiltonian is the potential of the electrons "tightly-bound" to each atomic site, the hopping potential can be treated as a perturbation. The discussion in this section is self-contained, but inspired by the lecture notes available online from Leggett [31].

Since electrons in graphene are tightly bound to the atoms, it is also possible to neglect all hopping except for to nearby atoms. For graphene, good agreement is achieved for the nearest neighbours only and the Hamiltonian for the hopping can be written in reciprocal space as:

$$\mathcal{H}_{\vec{k}}^{TB} = -\gamma_0 \left(e^{-i\vec{\delta}_1 \cdot \vec{k}} + e^{-i\vec{\delta}_2 \cdot \vec{k}} + e^{-i\vec{\delta}_3 \cdot \vec{k}} \right) a_{\vec{k}}{}^{\dagger} b_{\vec{k}} + H.C. \tag{1.1}$$

Where $\gamma_0 \approx 2.8\ eV$ is called the hopping parameter and the creation and annihilation operators $(a_{\vec{k}}^{\dagger}, b_{\vec{k}}^{\dagger}, a_{\vec{k}}, b_{\vec{k}})$ represent the plane-wave electron states on the A sublattice and the B sublattice [10]. This can be simplified as the matrix:

$$\mathcal{H}_{\vec{k}}^{TB} = \begin{pmatrix} a_{\vec{k}}^{\dagger} & b_{\vec{k}}^{\dagger} \end{pmatrix} \begin{pmatrix} 0 & \Delta^* \\ \Delta & 0 \end{pmatrix} \begin{pmatrix} a_{\vec{k}} \\ b_{\vec{k}} \end{pmatrix} \tag{1.2}$$

Where $\Delta = -\gamma_0 e^{-ik_x a}\left(1 + 2e^{i\frac{3}{2}k_x a}\cos\left(\frac{\sqrt{3}}{2}k_y a\right)\right)$. Taking the determinant gives the energies:

$$E_{\vec{k}} = \pm\gamma_0\sqrt{1 + 4\cos\left(\frac{3}{2}k_x a\right)\cos\left(\frac{\sqrt{3}}{2}k_y a\right) + 4\cos^2\left(\frac{\sqrt{3}}{2}k_y a\right)} \tag{1.3}$$

The system has two non-overlapping energy bands shared by two free electrons. When the system is charge neutral, there should be one band each completely full and completely empty.

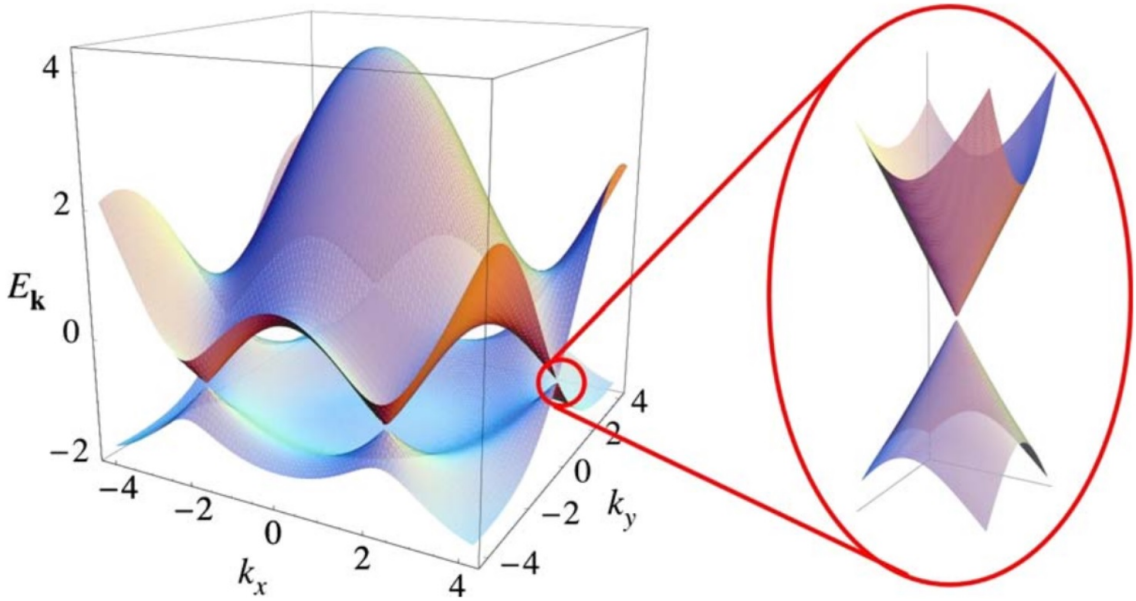

Figure 1.7: Band structure of monolayer graphene.
The low-energy physics takes place at the maximum symmetry points where the allowable states are described by a cone. This figure is reproduced from a review by A. Castro Neto et al. [10].

The bands touch at the $\vec{K}$ and $\vec{K}'$ points, so this is where the low energy physics should take place. Expanding Δ about $\vec{k} = \frac{2\pi}{3a}\left(1, \pm\frac{1}{\sqrt{3}}\right) + \vec{q}$ gives:

$$\Delta = -\frac{3at}{2}\left(e^{i\frac{5\pi}{6}}\right)(k_x \pm ik_y) \tag{1.4}$$

The phase does not affect the physics. In terms of the Pauli spin matrices and the Fermi velocity $v_F = \frac{3a\gamma_0}{2\hbar} \approx 1.0 \times 10^6 \ \frac{m}{s}$, the low-energy Hamiltonian is:

$$\mathcal{H} = \hbar v_F \vec{\hat{\sigma}} \cdot \vec{k} \tag{1.5}$$

This is the form of the Dirac Hamiltonian for a massless 2D spin-$\frac{1}{2}$ particle, where valley ($\vec{K}$ or $\vec{K}'$) plays the role of spin.

In AB-stacked bilayer graphene (refer to Figure 1.6), the first order Hamiltonian is two monolayer graphene subspaces coupled only from a^{bot} to b^{top} as follows:

$$\mathcal{H} = \begin{pmatrix} a_{\vec{k}}^{top\dagger} & b_{\vec{k}}^{top\dagger} & a_{\vec{k}}^{bot\dagger} & b_{\vec{k}}^{bot\dagger} \end{pmatrix} \begin{pmatrix} 0 & \Delta^* & 0 & 0 \\ \Delta & 0 & \gamma_1 & 0 \\ 0 & \gamma_1 & 0 & \Delta^* \\ 0 & 0 & \Delta & 0 \end{pmatrix} \begin{pmatrix} a_{\vec{k}}^{top} \\ b_{\vec{k}}^{top} \\ a_{\vec{k}}^{bot} \\ b_{\vec{k}}^{bot} \end{pmatrix} \tag{1.6}$$

Where $\gamma_1 \approx 0.1\gamma_0$ is the interlayer hopping parameter [32]. Since we are most interested in the physics when Δ is near zero (the so-called "Dirac" point), this first order, nearest neighbour description is inadequate (the matrix becomes singular). The full resolution of this problem involves solving a 4×4 matrix with four hopping amplitudes [32]. The fundamental idea, however, can be seen by considering the hybridized bands due to the inter-layer hopping term γ_1. The $b^{top} - a^{bot}$ subspace generates two hybridized bands with energy $E = [0, \gamma_1]$. When Δ is small relative to γ_1, one of these bands will always be filled and one of these bands will always be empty. Accordingly, we can consider only what is going on in the $a^{top} - b^{bot}$ subspace. We need to consider electrons which hop from a^{top} to the b^{top} part of the unfilled

hybridized band (amplitude Δ), and then from the a^{bot} part of the hybridized band to b^{bot} (amplitude Δ). The hopping is suppressed by the energy of the intermediate state (γ_1), resulting in the following effective Hamiltonian at low energies:

$$\mathcal{H} = \begin{pmatrix} 0 & \frac{\Delta^2}{\gamma_1} \\ \frac{\Delta^{*2}}{\gamma_1} & 0 \end{pmatrix} = \frac{\hbar^2 v_F^2}{\gamma_1} \begin{pmatrix} 0 & (k_x + ik_y)^2 \\ (k_x - ik_y)^2 & 0 \end{pmatrix} = \frac{\hbar^2}{2m_{eff}} \left(\vec{\hat{\sigma}} \cdot \vec{k}\right)^{\circ 2} \tag{1.7}$$

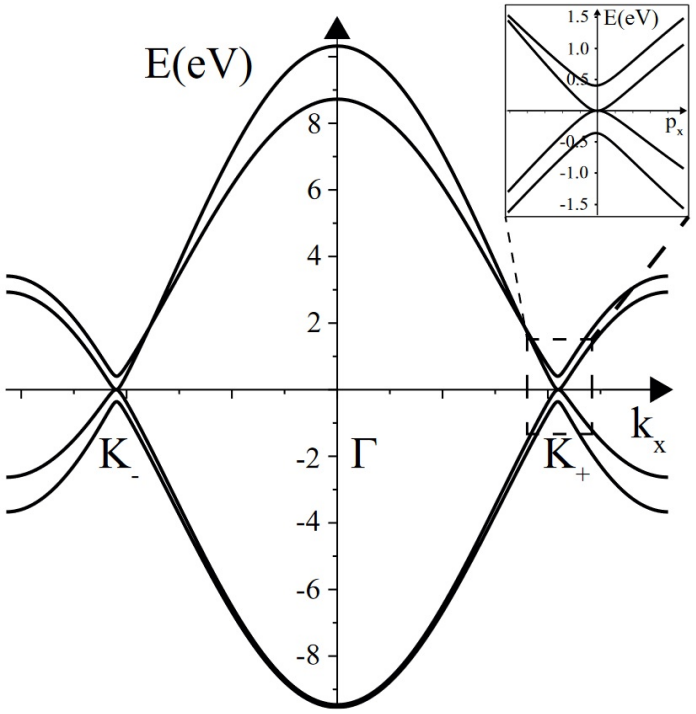

Figure 1.8: Electronic dispersion in bilayer graphene.
E vs k_x) for bilayer graphene. Lattice basis with twice as many atoms as monolayer giving twice as many bands. Moreover, in bilayer graphene, the band structure is quadratic at low energy and the carriers resemble "massive" Dirac Fermions. This figure is reproduced from a review by E. McCann [32].

Where $m_{eff} = \frac{\gamma_1}{2v_F^2}$ is the effective mass of the electrons at the CNP. Note that $\hat{A}^{\circ 2}$ denotes the Hadamard or element-wise square of $\hat{A}$. The electronic dispersion in bilayer is illustrated in Figure 1.8. Bilayer graphene has parabolic dispersion at low energy. This increases the density of states near the Dirac point, making the physics

there more robust to charge density fluctuations. This also affects the winding number and the so-called "Berry Phase" (equal to π in graphene and 2π in its bilayer) [33]. There are also two additional bands at energy $E = \pm\gamma_1$ which can couple strongly to the mechanics [34]. Since the wavefunctions of the electronic states are substantially different, the electronic properties are similarly affected.

The electrons in bilayer graphene are said to be "massive" Dirac Fermions because of their dispersion. The band structure of bilayer graphene is similar to monolayer, with the key difference that the dispersion near the Dirac point (below $\approx 5\ meV$) becomes quadratic [35]. In this sense, low-energy electrons in bilayer graphene are "massive" Dirac Fermions described by Equation 1.7 [35].

Away from the Dirac Point, the 2D structure and linear density of states leads to conductivity which is proportional to charge density (see Equation 1.8) [36].

$$G_0 = \frac{W}{L} ne\mu \tag{1.8}$$

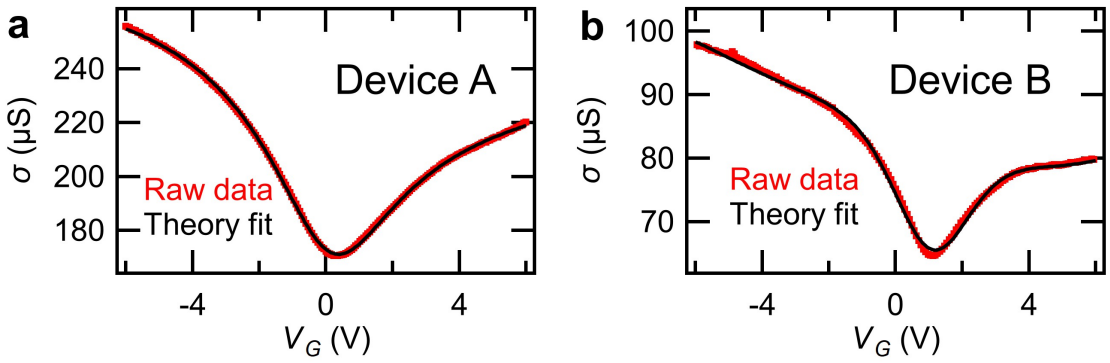

Figure 1.9: DC conductivity ($\sigma = \frac{L}{W}G$) data for a bilayer graphene device. The bottom axis is the gate voltage used to control the charge density and the left axis is the conductance. Mobility and contact resistance can be extracted by fitting the data [37].

Where G_0 is the conductance of the bare device, n is the charge density, and μ is a constant called mobility. For a real device, we need to account for impurities and contact resistance [38]. The measured conductance (G) is determined by the

conductance of the channel (G_0) and contact resistance R_c. Since the sample is truly two-dimensional, the charge density can be varied capacitively via the gate voltage (V_G). Charge density in graphene is also influenced by temperature and impurities. Finally, hole density and electron density can be described by a Fermi function.

This description is sufficient to understand the DC conductance data in real electronic devices made from monolayer and bilayer graphene. An example of such data is shown in Figure 1.9, showing one of our bilayer graphene samples which can be analyzed to extract contact resistance (R_c), mobility (μ), and other quantities. With this understanding of the electronics, it becomes possible to identify signatures of the mechanical behaviour in the electronic data.

1.3.3 Mechanical Excitation of 2D Carbon NEMS in the Quantum and Classical Regimes

The mechanical excitations of pristine 2D carbon NEMS can be described by their phonon dispersion (quantized atomic-level vibrational modes), as well as their macroscopic vibrational modes. Due to the conservation of momentum, a major source of electronic resistivity arises from collisions between charge carriers and phonons. It is important to know which phonons exist in graphene.

Despite having 2D electronic states, these materials exist in 3D, leading to six phonon modes [39] (the additional two modes are quadratic out-of plane modes). The phonon dispersion can be seen in Figure 1.10. Some of the optical phonon modes can be probed by Raman spectroscopy [40].

The relative amplitudes of Raman processes are highly sensitive to interlayer interactions. The shape and relative intensity of the various Raman peaks can be used to determine layer number, as demonstrated in Figure 1.11.

Suspended bilayer graphene is not an infinite crystal, so it also has macroscopic mechanical modes called vibrons determined by its length, width, and boundary conditions [41]. The mechanics of linear mechanical modes are described by a second

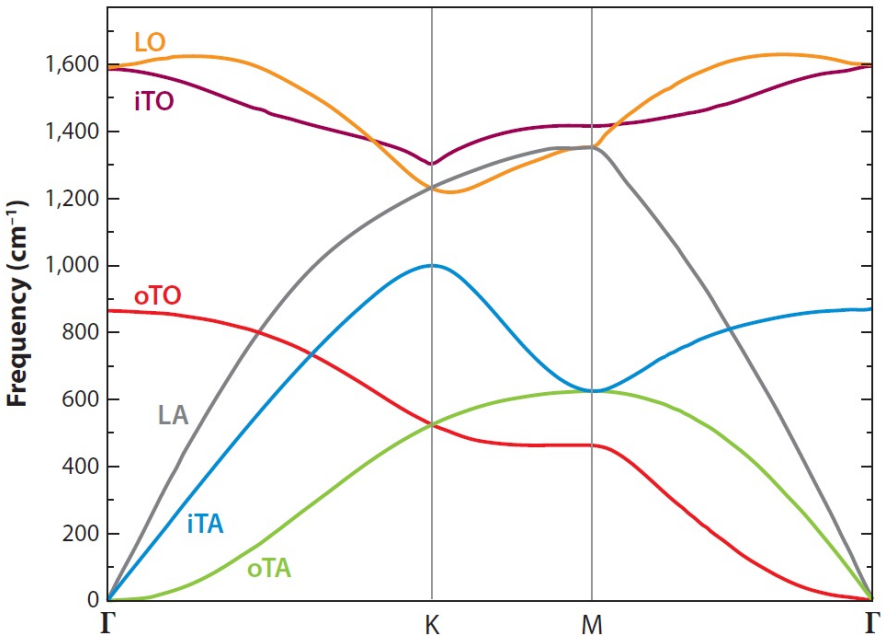

Figure 1.10: The phonon modes of graphene.
While graphene electrons are 2D, we measure it in three-dimensional (3D) space. This gives graphene (with a two atom basis) the usual 4 phonon modes (two acoustic plus two optical) for 2D, and an additional two out-of-plane phonon modes (one acoustic, one optical). The same modes are present in bilayer graphene with modified frequency. This figure was reproduced from a review by M. Dresselhaus et Al. [39].

order linear differential equation:

$$\ddot{z} + \frac{\omega_0}{2Q}\dot{z} + \omega_0^2 z = \frac{F}{m_{eff}} cos(\omega t) \tag{1.9}$$

Where z is the mechanical displacement, Q is the quality factor and commonly reported as the full width at half max divided by the frequency, ω_0 is the angular frequency at resonance, controlled by the elastic modulus and the tension, and F is the maximum amplitude of the sinusoidal driving force. The line shape of the resonance is given by a Lorentzian [14] as described by Equation 1.10. If F is due to capacitive coupling to a gate, it is proportional to the square of the drive voltage by the usual relation $F_{cap} \propto C^2V^2$.

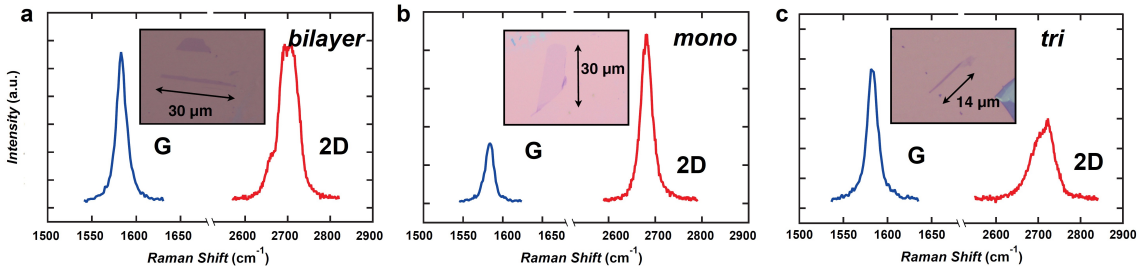

Figure 1.11: Raman modes in bilayer graphene compared to those in monolayer and trilayer.
The effects of increasing layer number on Raman spectrum. **a** bilayer graphene **b** monolayer graphene and **c** graphite. As layer number increases, the second order G peak (red) splits and the first order D peak (blue) becomes more important. This figure was reproduced from a thesis by S. Yiğen [37].

$$\delta z = \sqrt{\frac{F}{m_{eff}}} \sqrt{\left(\left(\omega_0^2 - \omega^2\right)^2 + \left(\frac{\omega\omega_0}{2Q}\right)^2 \right)^{-1}} \tag{1.10}$$

Where δz is the amplitude of the sinusoidal mechanical response. Q describes describes the lossiness of the resonance, and $\omega_0 = \sqrt{\frac{k}{m}}$ where k is the spring constant and m is the effective mass (details in Chapter 3). NEMS resonance can be explored in suspended graphene sheets by electronic actuation of the sheet mechanical resonance. Q for low-disorder monolayer graphene NEMS can be as high as 2.45×10^5 [42]. Due to their high quality factors, these modes generate a large out-of-equilibrium population of out-of-plane acoustic vibrons.

Realistic sheet NEMS also exhibit more complex mechanics because of effects such as wrinkling (static surface corrugations) and rippling (time-dependant surface corrugations) [43].

1.3.4 Bilayer Graphene Nanoelectromechanical Systems

A suspended bilayer graphene sheet can be deflected by an applied gate voltage via a force due to electrostatic coupling (see Figure 1.12).

The gate voltage also controls the charge density and therefore the conductivity.

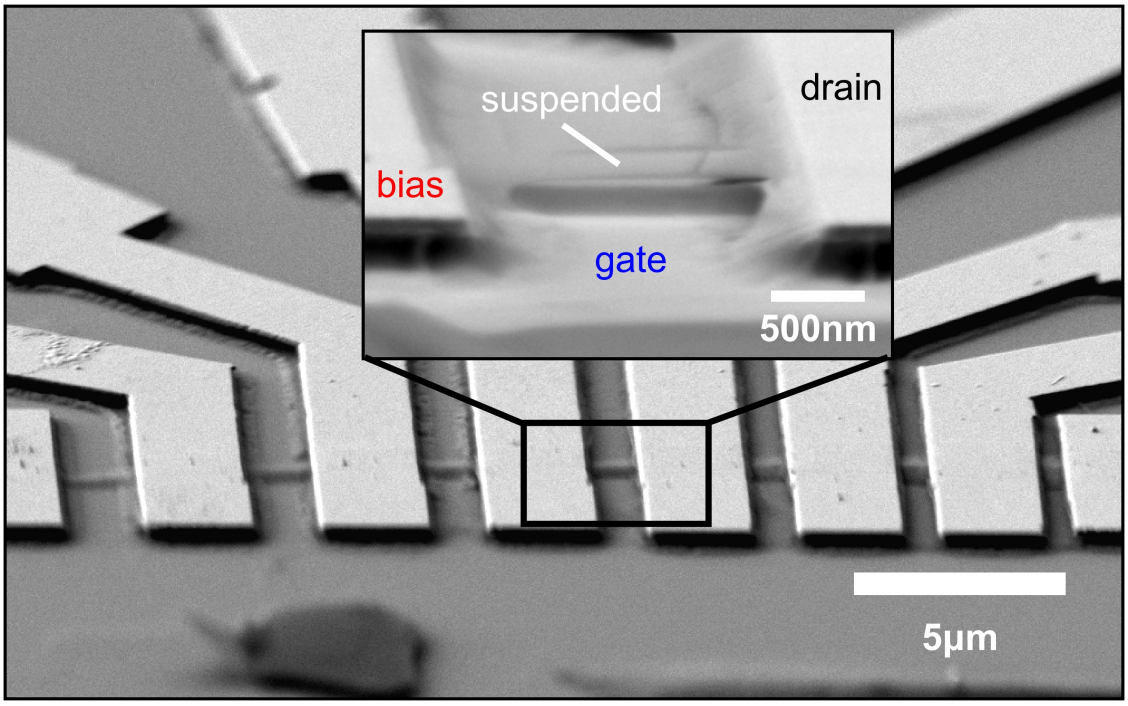

Figure 1.12: Capacitive gate coupling to a bilayer graphene electromechanical resonator.
A doubly clamped rectangular graphene membrane on an SiO_2 substrate suspended above a global back gate.

Both of these effects are mediated by the capacitance between the gate and the bilayer graphene sheet. Varying the height of the bilayer graphene sheet (a mechanical degree of freedom) above the gate electrode varies the capacitance and couples the mechanics into the electronics.

1.4 Outline of this Thesis

Our three main results are: development, deployment, and fine-tuning of the samples, methods, and platform for the simultaneous DC and RF characterization of low-disorder BG-NEMS; the detection of BG-NEMS resonance at MHz frequencies; and reporting of tunable resonance, amplitude, quality factor, and morphology in BG-NEMS.

In Chapter 2, we report our fabrication methods for low-disorder BG-NEMS. The

fabrication process to isolate low-disorder crystalline bilayer graphene with lengths of around 1 μm is described. We also developed measurement methods to directly measure, optimize, and characterize the resonance. An annealing process is described which can achieve impurity charge density as low as $n \approx 10^9\ cm^{-2}$, this corresponds to $E_F = n \times \pi\hbar^2 \times \frac{v_F^2}{\gamma_1} \approx 1.8\ meV$ or about 21 K (calculated using the density of states [32]). In the annealed samples, a high-frequency current mixing circuit is demonstrated which can resolve conductivity fluctuations due to resonance. The current mixing signal is used to find and probe the electromechanical resonance in our suspended bilayer graphene samples.

In Chapter 3, a study of the properties of bilayer graphene electromechanical resonators. The frequency, quality factor, and amplitude of the resonance can be directly extracted from the mixing data. Frequencies range from 130 MHz to 220 MHz. We extract quality factors up to ≈ 2000. A gap in the resonance frequency is observed versus strain. At higher drive powers, Duffing nonlinearity is observed. The nonlinearity is the correct magnitude to explain the frequency gap as mode mixing between a wrinkled conformation and a membrane conformation of the resonating membranes. Large negative differential mobility is observed near the frequency gap. Suppression of mobility is consistent with a picture where surface variations induce doping disorder. Negative nonlinear damping is also present despite not being predicted from a geometric description of the oscillator. Nonlinear losses are also present in the devices. Morphological disorder is proposed as a source of these nonlinear losses. We posit that the nontrivial morphology is a result of a fabrication process which takes place at different temperature than the measurement.

In Chapter 4, we summarize the major results of this thesis. Furthermore, we conclude with a list of questions raised by this thesis and its implications for future study of bilayer graphene NEMS.

Chapter 2

Methods to Explore Bilayer Graphene Electromechanical Resonances

This Chapter describes the methods we used to fabricate and study electromechanical resonances in bilayer graphene samples. These methods are based off of those previously used to study monolayer graphene NEMS. We made several unique optimizations to enable our measurement.

Bilayer graphene samples exfoliated from highly ordered pyrolitic graphite were used to eliminate the lattice disorder associated with chemical vapour deposition. Samples were fabricated to dimensions of approximately 1 μm to accommodate for for the issues of collapse and low quality factor at larger samples as well as poor annealing and small signal size for smaller samples. Current annealing was used to bring the samples as close as possible to ideal bilayer graphene sheets. Finally, a highly-tuned mixing measurement was made to allow resolution of signals smaller than 1 pA.

Electromechanical resonance in bilayer graphene NEMS (BG-NEMS) is a coupling between the mechanical displacement and the electronic transport through the capacitance. In our system, charge oscillations induced by a gate electrode exert

a force which drives the oscillations of the tension and the out-of-plane displacement of the sample.

In Section 2.1 we present the fabrication (see Figure 2.3) of electromechanical resonators actuated by capacitive coupling of a doubly-clamped suspended bilayer graphene transistor. In Section 2.2 we present an annealing procedure to remove doping impurities absorbed on the channel. In Section 2.3, the mixing RF current measurement whereby the BG-NEMS can be actuated and detected is discussed.

Since the electrical impedance between the channel and the back gate substrate (doped Si) is frequency dependent ($Z_C = \frac{1}{\omega C}$ where $\omega = 2\pi f$), we expect channel–back-gate to be shorted at high frequency. The solution used in this work is to perform a mixing measurement between the source and gate signals. The detection is made at a lower frequency equal to the difference in frequency (Δf) between the signals on the source and gate.

2.1 Microfabrication of Suspended BG-NEMS

Doubly clamped resonators can be fabricated by the following procedure [44]:

- Highly-crystalline bilayer graphene samples are exfoliated onto an SiO_2 substrate prepared with a gold coordinate grid.
- Source and drain electrodes are lithographically defined (see Figure 2.2).
- The samples are liberated by wet-etching the SiO_2 substrate (see Figure 2.3).

Large scale growth of graphene layers can be accomplished using chemical vapour deposition and molecular beam epitaxy; however, 2D NEMSs with the highest mobility and lowest disorder must be produced by the so-called "Scotch Tape Method" whereby Highly-Ordered Pyrolitic Graphite (HOPG) is exfoliated (or "peeled") using adhesive tape until it has the desired range of thicknesses and then pressed onto the desired substrate.

The method used by our group is:

1. Start with as large as possible a flake of HOPG
2. Split the flake as thin as possible with clean tweezers and a razor
3. Place the flake onto about fifteen centimeters of scotch tape
4. Fold the two halves of the tape together and press out the air bubbles
5. Peel slowly to split the graphite onto both halves, repeat twenty times
6. Press the tape onto substrate and compress with a book for $\approx$ 5 minutes

Since exfoliated graphene is more-or-less randomly distributed, a photolithography mask is used to pre-pattern chips with gold alignment marks to allow candidate flakes to be easily located once found. Each graphene layer absorbs roughly 2.3% of light (and significantly more when placed on a 300 nm SiO_2 substrate) allowing reasonably good identification of candidate bilayer graphene using optical microscopy (see Figure 2.1). On our substrates of metallic sillicon covered in 295 nm of SiO_2, this results in a characteristic deepening of the "blue" oxide as can be seen in Figure 2.1. Once candidate chips have been established, their layer number is determined by looking at the second order 2D peak of the Raman shift (as described in Figure 1.11).

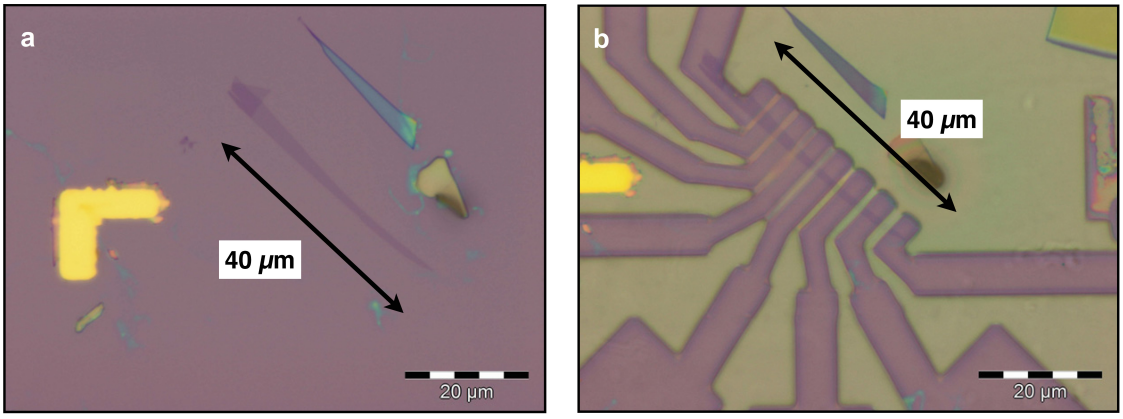

Figure 2.1: Alignment and lithography to define bilayer graphene transistors. **a** Bilayer graphene (darker blue) is identified under a microscope (confirmed afterwards with Raman spectroscopy). **b** Bilayer graphene transistors are defined by electron beam lithography in a layer of resist.

BG-NEMS are fabricated by suspending a bilayer graphene crystal between two gold electrodes (doubly clamped geometry) above a gate electrode. The resonator

lengths needed for this experiment are between 1-2 μm. Long devices collapse at much lower gate voltages, making the measurement unfeasible. Shorter devices are much harder to anneal because they are nearly ballistic (heat is localized at contacts). To make devices of these dimensions, electron beam lithography with an MMA/PMMA bilayer resist is used to define source/drain electrodes and contact pads onto which 3 nm chrome and 120 nm gold are evaporated. This process is illustrated in Figure 2.2.

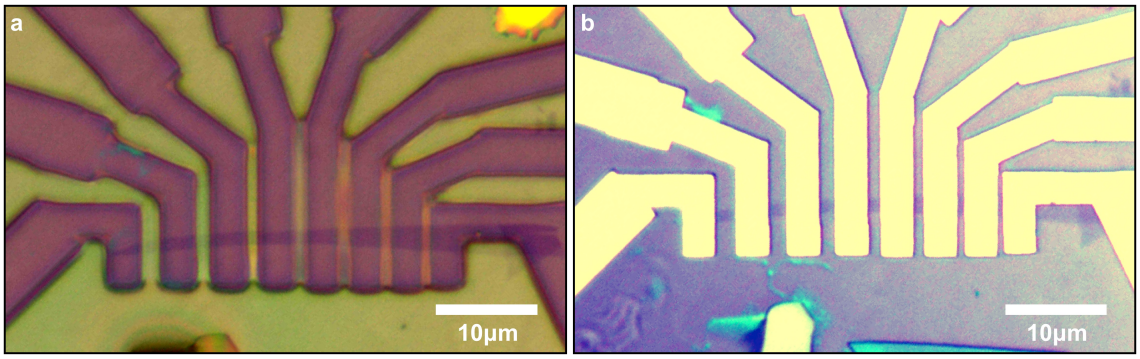

Figure 2.2: Evaporation of gold electrodes.
a Electron beam lithography is used to define a negative pattern of the desired electronic contacts in resist (large purple structures). The candidate devices occur in random positions and orientations, so alignment of the lithography design and the graphene flake is acheived with the aid of a gold grid deposited beforehand. **b** Gold contacts (in yellow) are evaporated onto the sample to define the channel length. [44]

HF buffered oxide etch is used to remove about 200 nm of oxide in order to suspend the sample. Surface tension can cause the samples to collapse as they dry [45], so they are dried in a critical point dryer.

Suspension can be confirmed by analysis with either AFM or SEM, although these are usually done after experimental measurements because the analysis can damage the sample [12]. Suspended devices, with suspension confirmed from a tilted SEM image can be seen in Figure 2.3. The desirable electronic features of a bilayer graphene transistor are high mobility and a charge neutrality point near zero. These properties are illustrated in Figure 2.4.

After fabrication, our suspended bilayer graphene transistors are not yet ready for measurement. Firstly, their surface is contaminated by water and nanofabrication residues. Without further processing, they have limited charge mobility and

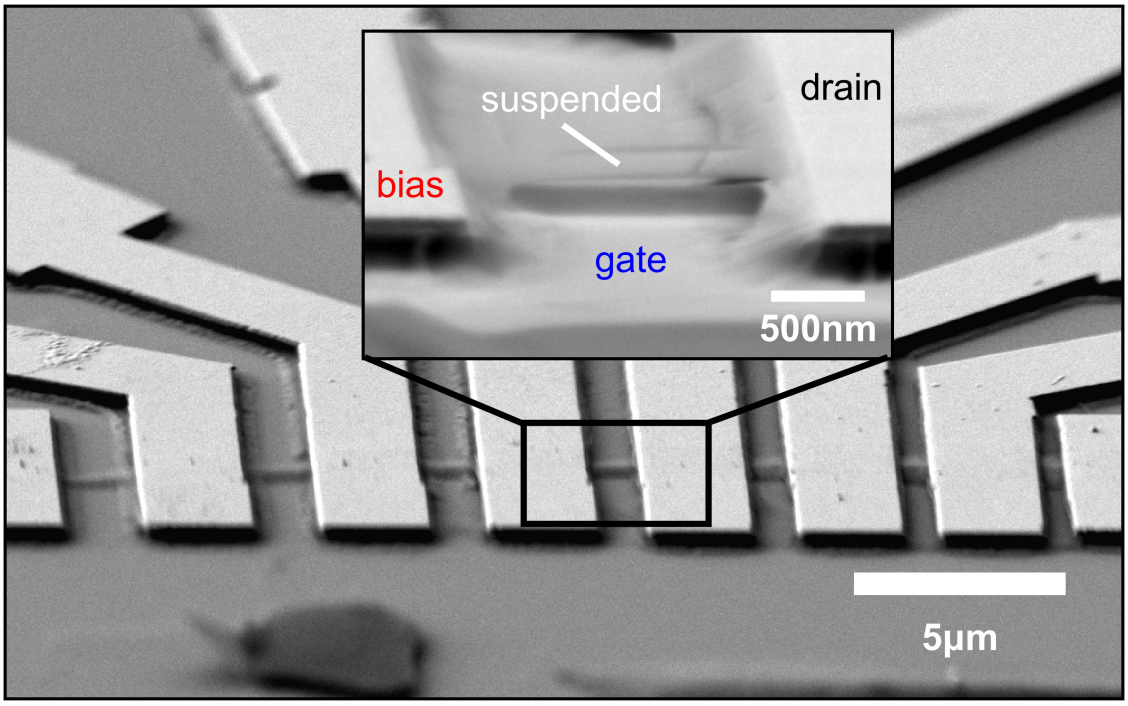

Figure 2.3: SEM imaging of suspended BG-NEMS.
After measurement, the suspension of the sample can be confirmed with SEM. When the tilt angle is high enough, an image showing full suspension can be acquired (inset).

inhomogeneous charge density. Moreover, the impurity charge density is too large to see the charge neutrality point. Once the samples have been liberated from the substrate, however, it is possible to anneal them by flowing a large annealing current which must dissipate in a cross section only two atoms thick.

2.2 Annealing to Ultra-Low Disorder

Since graphene's sp_2 carbon bonds are extremely robust, bilayer graphene crystals can withstand temperatures approaching that of the surface of the sun (4500 Kelvin) [46]. At such temperatures and under high vacuum ($P \lesssim 10^{-6}$), water is desorbed and polymer residue is ashed off. The heating is accomplished by passing a large current through the samples and is called Joule annealing [47].

To perform current annealing, we built a feedback-controlled circuit which can monitor source-drain current. Computer feedback makes the process more repeatable

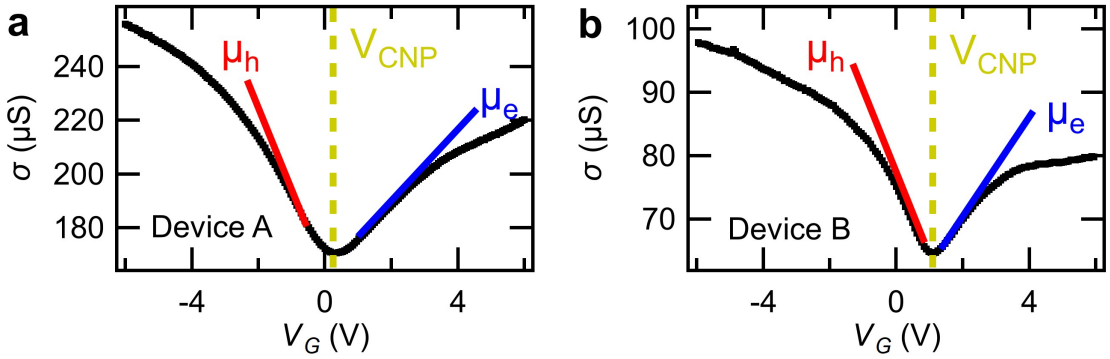

Figure 2.4: Illustrating the desired μ and V_{CNP} in DC data.
Carrier mobility (μ_e for electrons and μ_h for holes) describes the conductivity (σ) increase as charge carriers are added (deviations from a line are due to contact resistance R_C). The minimum of the conductivity occurs at the minimum of the charge density (charge neutrality point V_{CNP}). To perform the measurement, we want high μ and accessible V_{CNP}.

through high sensitivity manual control of the voltage ramp and hold rates. Large changes in resistance also trigger an automatic safe rampdown.

As seen in Figure 2.5 (panels **b**, **c**, and **d** at high currents), saturation (flattening) of the Ohmic response of the device indicates that the device has begun to anneal. Care must be taken however, as this is also the regime where you need to worry most about device failure however. In this regime, annealing power should be increased in small steps. Between the steps, DC characteristics are measured. Once the Dirac point is visible, significant change between anneals indicates that a measurement should be attempted before continuing. Figure 2.5 shows the effects of annealing on our sample.

Annealing improves two features of the $I-V_G$ data shown in Figure 2.5 (panels **e**, **f**, **g**, and **h**). First, the charge neutrality point (conductance minum) moves towards 0 V as the impurity charges are burned off. Second, as the disorder decreases, the mobility increases, leading to steeper slope as you approach the charge neutrality point. The measurement sensitivity is proportional to responsiveness of the conductivity to a varying charge density, as characterized by the mobility. This step is important because the device fabrication exposes the graphene to glue, resist, and moisture

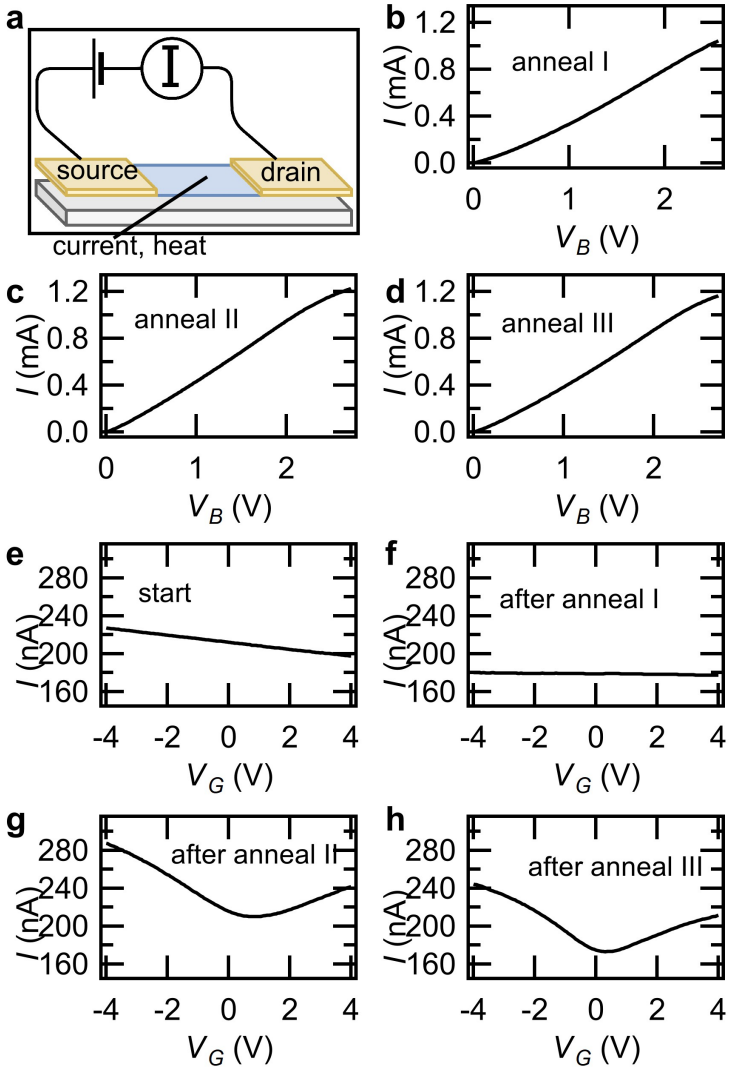

Figure 2.5: Joule annealing of BG-NEMS. **a** *Circuit schematic* Source and drain are gold, sample is blue. **b,c,d** *Annealing data* Deviations from the line $V_B = IR$ occur in the annealing regime (high V_B). **e,f,g,h** *Improvement after annealing* Anneals reduce doping (lower I_{CNP}, $V_{CNP} \to 0$) and increases mobility (higher slope). Data from Device A.

resulting in charged, low-mobility samples.

Annealing also presents a significant risk of device failure (see Figure 2.6). Since changes in resistance at a given voltage can lead to large changes in annealing power, it is important to anneal slowly. Computer control of the annealing circuit aids with this issue, but does not eliminate it entirely.

After the annealing has improved our mobility to approximately the 50 000 cm^2/Vs range (at a temperature of 4 Kelvin), it becomes possible to search for the electromechanical resonance via a mixing measurement. This device quality is required because the current mixing is proportional to the derivative of the $I - V_G$

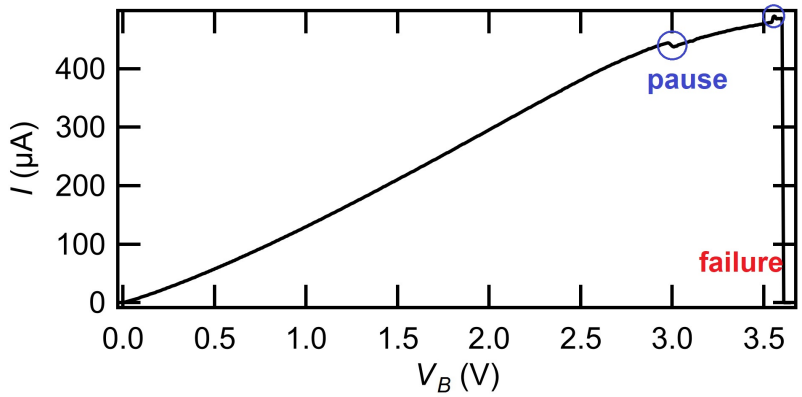

Figure 2.6: Catastrophic device failure during annealing.
$I-V_B$ data in a device destroyed by current annealing. Rapidly changing conductivity can cause uncontrolled current increases which destroy the device.

data.

2.3 Mixing Source and Gate Signals

Mixing current measurement is a low-noise technique to measure the slope of the $I-V_G$ data. The technique is also sensitive to mechanical resonance. To observe BG-NEMS resonance, however, the circuit must be specially designed to accommodate the radio frequency (RF) resonance. Furthermore, detection of mechanical resonance in bilayer graphene is more difficult than in monolayer because the conductance minimum is less sharp, the mobility is somewhat lower, annealing is harder, and disorder has a greater impact on the device performance.

2.3.1 DC Conductivity Model in Bilayer Graphene

The conductivity of a bilayer graphene transistor cannot be described satisfactorily using the channel conductivity $\sigma = ne\mu$. In our devices, there is a large contact resistance (R_C) between the gold electrodes and the bilayer graphene sheet. Furthermore, the mobility of the electrons is not the same as for holes (particularly at low temperatures). The goal of this section is to present a model of the DC electronics that is sufficient to fit to our DC data and aid in understanding of the electronics at

higher frequencies.

The conductance of the device is the conductance of the channel added in parallel with the conductance of the contacts.

$$G = \left(R_c + G_0^{-1}\right)^{-1} \tag{2.1}$$

Where R_c is the contact resistance and $G_0 = \frac{W}{L}\sigma$. The measure of quality of a DC transistor is typically given as a mobility (μ), which is related to the conductivity as:

$$\mu = \frac{\sigma}{ne} \tag{2.2}$$

Where e is the elementary charge. In a 2D semiconductor, the gate doping can be determined by assuming that the device is a parallel plate capacitor.

$$n_G = \frac{c_G}{e}\left(V_G - V_{CNP}\right) \tag{2.3}$$

Where c_G is capacitance per unit area and V_{CNP} is the gate voltage at the charge neutrality point. The conductivity minimum determines the charge neutrality point in bilayer graphene. In our devices, the capacitance is the series capacitance of the oxide and the air gap, which can be modelled as parallel plate capacitors since the graphene width is much greater than the suspension height.

$$c_G \approx \epsilon_0 \left(h_{suspended} + \frac{h_{SiO_2}}{\epsilon_{SiO_2}}\right)^{-1} \tag{2.4}$$

Where ϵ_0 is the the permittivity of free space, ϵ_{SiO_2} is the relative dielectric constant of the substrate, $h_{suspended}$ is the suspension height, and h_{SiO_2} is the height

of the remaining (un-etched) SiO_2 substrate.

Charge density is partly controlled by the gate, but also partly controlled by thermal doping and impurities [48][49].

$$n_{e/h} \approx \frac{1}{2}\left[\pm n_G + \sqrt{n_G^2 + 4n_0^2}\right] \tag{2.5}$$

Where n_0 includes both impurity charges (reduced by annealing) and thermal charge carriers (reduced by lowering temperature).

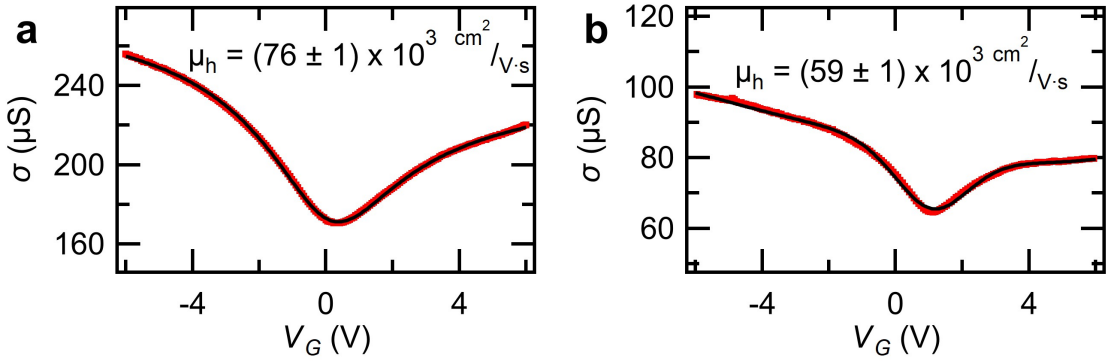

Figure 2.7: Extracting charge mobility, charge impurity density, and contact resistance for $\sigma - V_G$ data.
From Equation 2.6. Pictured: fits of conductivity versus gate voltage to extract mobility (overlaid, black) on the raw data (red dots), showing excellent agreement and great mobility in both **a** device A and **b** device B at T = 4 K. A mobility for holes has been extracted by fitting with Equation 2.6. Since the conductance minimum can be extracted without fitting and temperature is known, the only fit parameters are μ_e, μ_h, V_{eff}, and R_c.

These equations, when put together, allow for the determination of the mobility by the fitting following equation:

$$\sigma = \frac{L}{W}\frac{I}{V_B} \approx \left[\frac{W}{L}R_c + \left\{\left(\mu_e f_e(V) + \mu_h f_h(V)\right) c_G \sqrt{\left(V_G - V_{CNP}\right)^2 + 4V_{eff}^2}\right\}^{-1}\right]^{-1} \tag{2.6}$$

Where the impurities are captured by the V_{eff} and the difference between holes and electrons is captured by making the approximation $n_e = f_e n$ and $n_h = f_h n$, where f_e and f_h are the Fermi-Dirac function for holes and electrons respectively. This approximation is valid in bilayer because its density of states at low energy is constant [48].

An example of fitting the DC data with this equation and extracting mobility for holes and electrons is shown in Figure 2.7.

In devices outside the quantum regime with low disorder and negligible edge effects, a constant mobility is expected for electrons and another for holes.

Since the suspension height appears in the equation for capacitance, the conductivity fluctuations due to mechanical motion contribute to the mixing current. For a sufficiently large mobility and a sufficiently large-amplitude resonance, it should be possible to detect the resonance in the mixing current.

2.3.2 Low-Noise Current Mixing Measurement at Radio-Frequency

The following methods for detection of the mechanical resonance by mixing measurement follow those described by C. Chen et Al. [14]. Nonetheless, particular care had to be taken with the device geometry, annealing procedure, and circuit design in bilayer graphene.

Since the gate electrode is short-circuited to the sample at high frequencies, we measure at low frequency. The technique used is called current mixing. In a mixing measurement, the sample acts as a radio-frequency mixer between high frequency signals on the source $f + \Delta f$ and gate f, creating a signal on the drain electrode at the difference between them (Δf chosen to be easy to measure) [41]. The mixing is proportional to the fluctuation of the conductance δG due to the gate voltage. As shown in Equation 2.6, the gate voltage V_G varies the conductance G through the capacitance c_G. Since the capacitance depends on the suspension height, the mixing

current is also sensitive to mechanical motion at the drive frequency f, allowing the detection of the NEMS resonance (see Equation 2.7).

$$\delta G = \frac{\partial G}{\partial V_G}\left(\delta V_G + \frac{C'_G}{C_G} V_G \delta z\right) \tag{2.7}$$

Reflections off the sample also pose a problem [41]. Since the impedance of the coaxial cable is much smaller than the sample resistance, standing waves in the cable affect the voltage on the sample. This was solved by adding a capacitor and matching load in parallel, so that the radio frequency (RF) power is absorbed but the voltages still reach the sample.

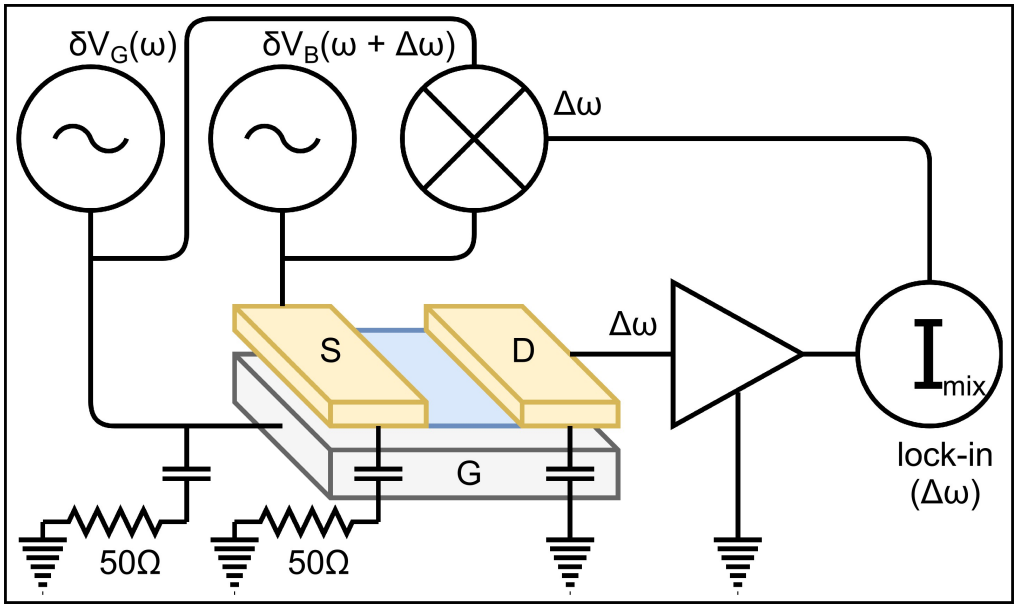

Figure 2.8: Simplified schematic of the RF mixing measurement circuit. Frequencies ω and $\omega + \delta\omega$ are administered to the gate (δV_G) and source (δV_B) electrodes respectively. At resonance, the motion of the graphene will modulate the capacitance and contribute an additional term proportional to the DC gate voltage (V_G). The low-frequency, mixed-down currents can then be detected by ordinary means. Tees block reflections from a large impedance mismatch for frequencies where $\frac{1}{\omega C} << 50\Omega$.

A circuit diagram illustrating the principal considerations is shown in Figure 2.8. The full circuit requires several additional components.

As shown in Equation 2.8, mixing is a high-resolution technique to measure the transconductance (derivative $\frac{dG}{dV_G}$ of the conductance G). Because of this, we can work backwards from the DC conductance measurements to verify whether our circuit is working.

The mixing response in our model mixes the voltage at the source with the charge density induced by the gate. The charge density varies by two mechanisms. Off resonance, the signal is due directly to the applied gate voltage (proportional to δV_G). Near resonance, another term due to the capacitance variation as the oscillator moves (proportional to δz) must be included [14]:

$$I_{mix}^{predicted} = \frac{1}{2}\delta V_s \frac{dG}{dV_G}\left(\delta V_G + \frac{C'_G}{C_G}V_G\delta z\right) \tag{2.8}$$

Where δV_s is the amplitude of the RF source voltage, δV_G is the amplitude of the RF gate voltage, V_G is the DC gate voltage, $\frac{dG}{dV_G}$ is the DC transconductance, $\frac{C'_G}{C_G}$ is the detection sensitivity, and δz_0 is the amplitude of the oscillation. And where the detection sensitivity is given by:

$$\frac{C'_G}{C_G} = \frac{dz_{avg}}{dz_{max}}\frac{c'_G(0)}{c_G(0)} = \frac{dz_{avg}}{dz_{max}}\left(h_{suspended} + \frac{h_{SiO_2}}{\epsilon_{SiO_2}}\right)^{-1} \tag{2.9}$$

For our mode shape, we assume the factor to be $\frac{dz_{avg}}{dz_{max}} = \frac{1}{2}$. The DC transconductance can be related to the nonresonance mixing current by the first term in Equation 2.8: $I_{mix}^{predicted} = \frac{1}{2}\frac{dG}{dV_G}\delta V_s \delta V_G$.

The detection of the small signals coming from the devices was enabled by a current preamplifier. Because of the background noise, a lock-in amplifier was also needed [50]. RF and DC generators were used to excite the devices.

Control of RF amplitude is accomplished with programmable attenuators. Bias tees are used on the source and gate; these enable DC and RF measurements in a single circuit. High pass filters and low pass filters were added in the appropriate

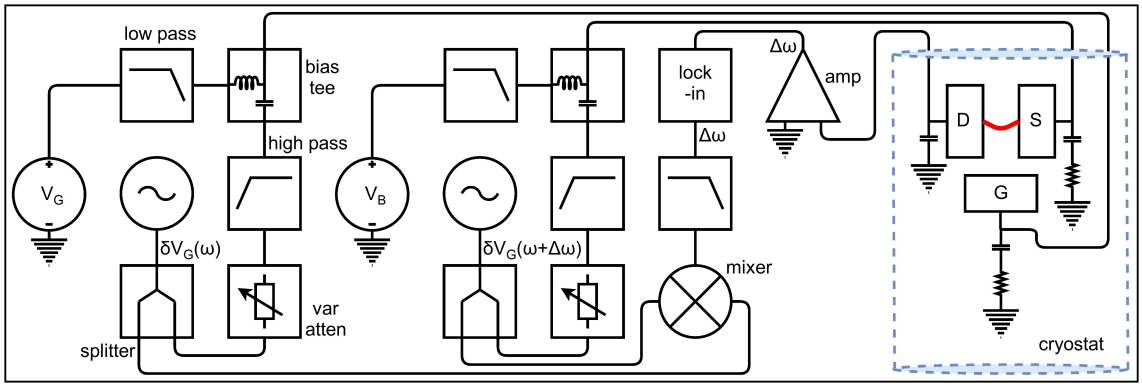

Figure 2.9: Detailed current mixing circuit schematic.
The circuit allows simultaneous control of DC and RF voltages. A current preamp and a lock-in amplifier are used to detect the small currents produced by the NEMS.

locations; these reduce noise and ensure the signal which is detected comes only from the sample. For the full circuit diagram, see Figure 2.9 and Table 2.1.

Part	Manufacturer	Part #
Bias Tees	Pasternack	PE1611
DC Blocks	Mini Circuits	BLK-89
Matching Loads	Mini Circuits	ANNE-50
Programmable Attenuators	Agilent (now Keysight)	J7211C
High Pass Filters	Mini Circuits	SHP-25
Low Pass Filters	Mini Circuits	BLP-1.9
RF Generators	Berkeley Nucleonics Corporation	BNC 3
DC Generators	Tektronix	Keithley 2400
Mixer	Mini Circuits	ZX05-10L
Splitters	Mini Circuits	ZFSC-2-4-S

Table 2.1: List of circuit components for RF mixing measurement of bilayer graphene NEMS in ^{4}He cryostat.

While the mixing circuit can only detect the mechanical motion on resonance, there is a background signal due to the first term in Equation 2.8. This contains useful information about the RF performance of the graphene transistor and also serves as a first demonstration of the circuit.

For any frequency at which the measured mixing current obeys the relationship in Equation 2.8 (where the $\frac{\partial G}{\partial V_G}$ term can be found from the DC $I - V_G$ data), we expect be able to measure a high-quality electromechanical resonance if it exists. As seen in

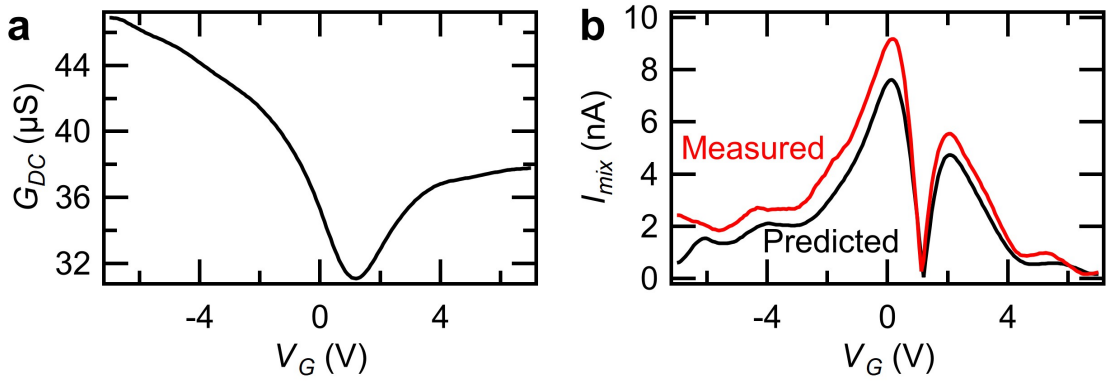

Figure 2.10: Test of agreement between measured I^{mix} and theoretical expectations. **a** The DC gate sweep data in Device B. **b** The measured mixing current (red) is compared to the predicted mixing current (black) based on the data in *a* using the Equation 2.7. Good agreement is obtained.

Figure 2.10, the mixing current measured with our circuit agrees very well with the mixing current predicted based on the DC data.

2.3.3 Advantages of Our Optimized BG-NEMS Measurement Platform

The major advantages of our measurement platform are threefold: annealing to resolve BG-NEMS mixing, single-circuit access to DC and RF data, and the access to simultaneous conductivity and resonance data.

Our carefully chosen device geometry allows us to anneal BG-NEMS which are nearly disorder free (charge mobility $\mu \approx 76000\, cm^2/Vs$, charge doping $n_0 < 6.6 \times 10^{-9}\, cm^{-2}$, mass density $\rho \approx 1.01\, \rho_{graphene}$). Moreover, the annealing can be accomplished with a single circuit. Accordingly, we are able to clean bilayer graphene sufficiently for mixing to be performed and then immediately measure it.

As the RF and DC data is taken with a single circuit, we are then able to compare the transconductance between a well-behaved DC setup and our experimental RF data. This feedback allows for calibration of the circuit and, most importantly, confirmation that our BG-NEMS are sufficiently annealed for measurement.

As the measurement is fundamentally electromechanical in nature, the same

data set allows for the extraction of electronic properties like mobility as well as the extraction of resonator properties like frequency, mobility, and amplitude. Importantly, this permits us to explore of the impact of the mechanical properties of our BG-NEMS on the electronics.

One final incidental advantage is the compatibility of the measurement with our existing fabrication procedure. Measuring directly at the resonance frequency requires additional fabrication steps (as shown in Figure 2.11).

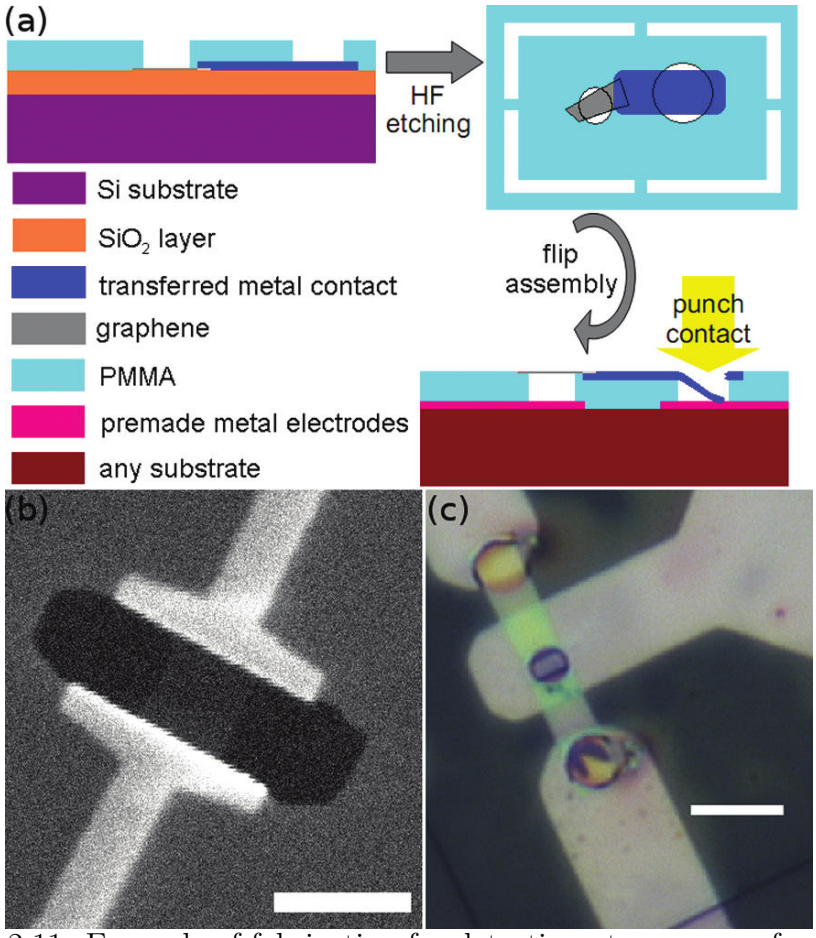

Figure 2.11: Example of fabrication for detection at resonance frequency. **a** A cartoon of the fabrication process. **b** Scanning electron microscope image of the device. **c** Microscope image of the gate. This figure is reproduced from a paper by Song et Al. [13].

The yield for our fabrication method (from identification to measurement) is on the order of 10%. Not only are these additional steps lower-yield, but they prevent

us from using our existing chip packaging system and preclude using our existing DC setup for magnetic field sweeps and temperature sweeps.

Chapter 3

High Quality Bilayer Graphene Electromechanical Resonators

This Chapter reports the detection of high-quality electromechanical resonances in BG-NEMS. We extract the frequency ($f \approx 135$ MHz and $f \approx 220$ MHz), quality factor (up to $Q \approx 2000$), and amplitude (δz from few pm to nearly 1 nm). These numbers are comparable to those reported in monolayer graphene [50]. The behaviour of the electomechanical resonances is explored at temperatures between 50 mK and 150 K with the majority of the data taken at 4 K under high vacuum.

First, we resolve the electromechanical resonance mixing at charge densities as low as $n \approx 10^8\ cm^{-2}$ thanks to the finite low-energy density of states for bilayer graphene, a major improvement over monolayer graphene. Next, the nonlinear properties of the resonances are explored at drive forces between $F \approx 5\mu N/cm^2$ and $F \approx 5N/cm^2$, revealing complicated nonlinear properties. The devices are doped with gate charge densities of up to $n_G \approx 10^{11} cm^{-2}$, resulting in a static strain force of 40 MN/cm^2. We measure high cooperativity nonlinear mode-mixing and quadratic gate hardening inconsistent with a membrane model. We describe these behaviours of our BG-NEMS in terms of rippled and wrinkled morphology.

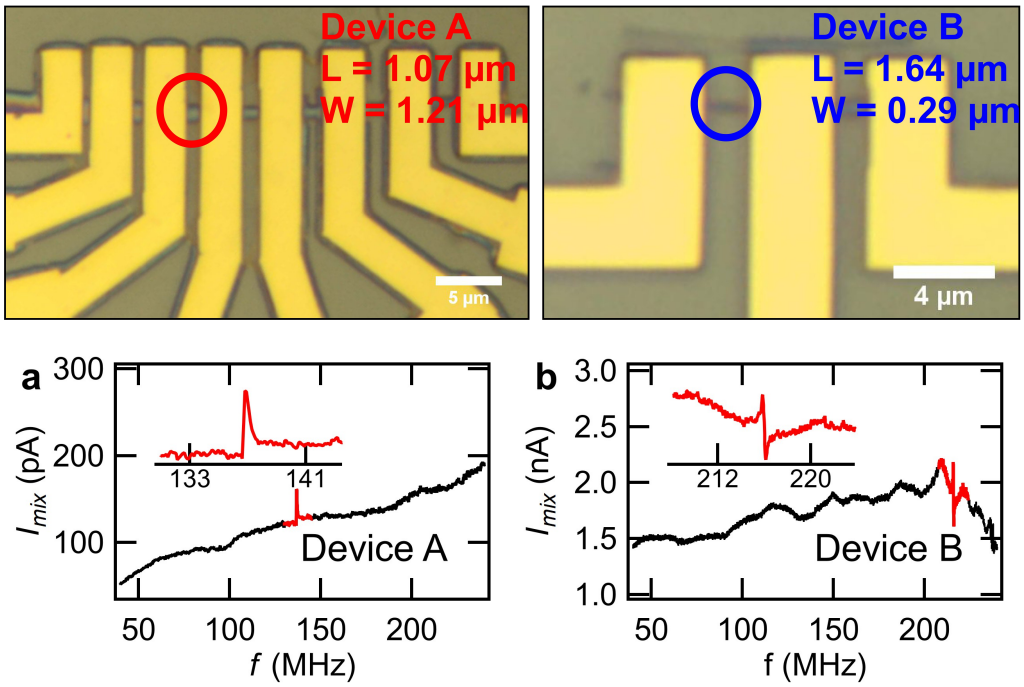

Figure 3.1: Observation of electromechanical resonance in devices A and B. Mixing current is measured vs the frequency at the gate. Making the measurement required good agreement between the DC gate sweep and the RF gate mixing sweep. Since the resonance frequency depends on geometry and built-in strain, it was essential to sweep a wide range of frequencies to find the resonance. To achieve a noise level which allows such sweeps to be taken in a reasonable amount of time, the following steps were taken: make the sweep at the best gate voltage (high $V_G \frac{\partial G}{\partial V_G}$), identify the lowest noise combination of source and gate voltage, and make the measurement at 4 Kelvin. The pictured flat frequency response was also needed to distinguish the resonance signals from the background. **a** device A. The data in device A was taken at $V_G = 3.2\ V$, $\delta V_B = 2\ mV$, and $\delta V_G = 1\ mV$. **b** device B. The data in device B was taken at $V_G = 2\ V$, $\delta V_B = 10\ mV$, and $\delta V_G = 20\ mV$.

3.1 Detection of Bilayer Graphene Electromechanical Resonances

With the devices and circuitry described in Chapter 2, it is possible to detect the small, high-frequency resonance signal. To understand our data we use a model that relates the shape of the resonance to its physically meaningful quantities such as the quality factor, the resonance frequency, and the amplitude of oscillation.

Although the shape of the resonance is indeed a Lorentzian, there is a phase

difference between the δV_G and δz, which must be accounted for in the fit $\tan(\phi) = (2Q)^{-1}\left(\frac{\omega_0}{\omega} - \frac{\omega}{\omega_0}\right)^{-1}$. To fit the frequency response, you need to treat the current as a phasor and add the phase-dependant contributions from the two terms.

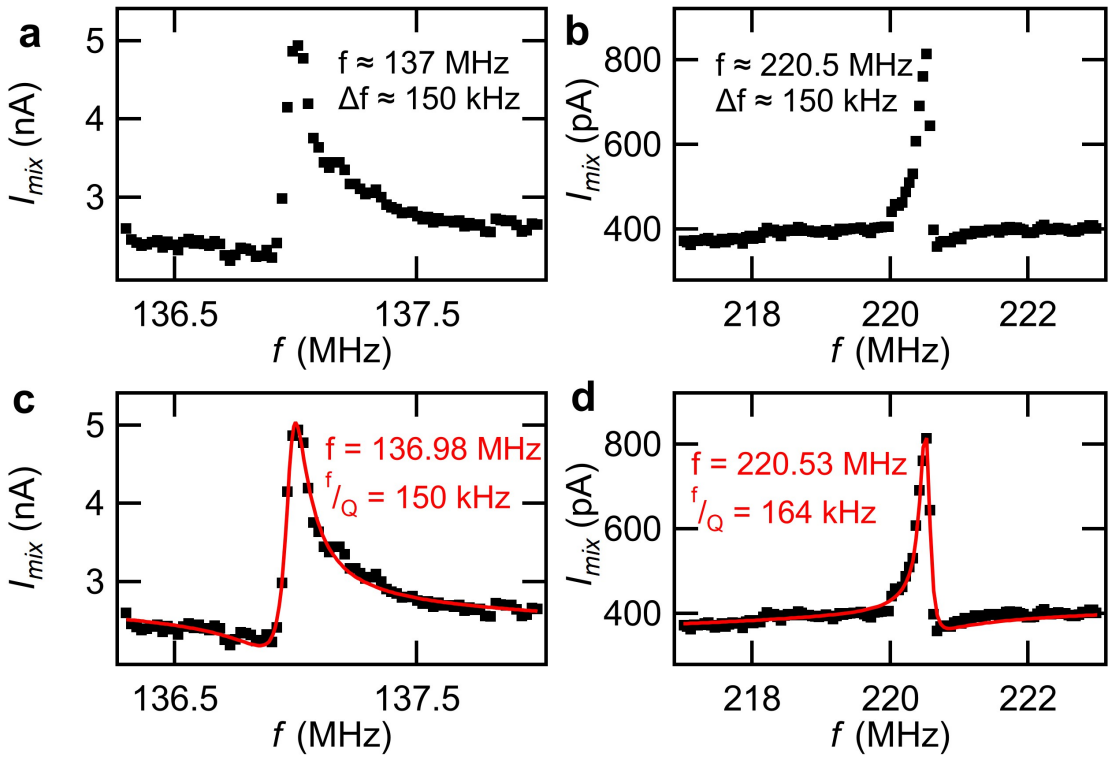

Figure 3.2: Electromechanical resonance line shapes.
a and **b** The frequency response in devices A and B respectively. The gate voltage is chosen so that the frequency and the resonance width can be easily estimated by eye. Essentially a close-up of Figure 3.1. **c** and **d** The model in Equation 3.1 is a good match for the shape and has good agreement with the estimated frequency and linewidth. Good agreement with the fit function adds confidence in the extracted parameters for less obvious lineshapes. The difference in frequency between this figure and Figure 3.1 is due to frequency tuning at the gate, as illustrated in Figure 3.11.

$$I_{mix}^{fit} = A + B\omega + I_{mix}^{resonance}\frac{\frac{\omega}{\omega_0}\cos(\phi) - (2Q)\left(1 - \frac{\omega^2}{\omega_0^2}\right)\sin(\phi)}{\frac{\omega^2}{\omega_0^2} + (2Q)^2\left(1 - \frac{\omega^2}{\omega_0^2}\right)^2} \tag{3.1}$$

Where ϕ is the phase between the mixing due to δV_G and δz [14]. Good agreement between this equation and the measurement suggests that the model can be trusted.

Moreover, the relationship between non-resonant mixing signal and the mixing signal due to resonance can be exploited in order to arrive at the following useful relation to extract the resonance amplitude from the fit:

$$\delta z = \frac{c_G}{c_G'} \frac{I_{resonance}^{mix}}{A + B\omega_0} \frac{\delta V_G}{V_G} \tag{3.2}$$

We also observe good quality factors in the ($Q \approx 1\,000$) range at 4 K. The resonance frequency of our oscillators is comparable to those of monolayer graphene resonators from previous works. We are also able to observe resonances up to 160 K (see Figure 3.3).

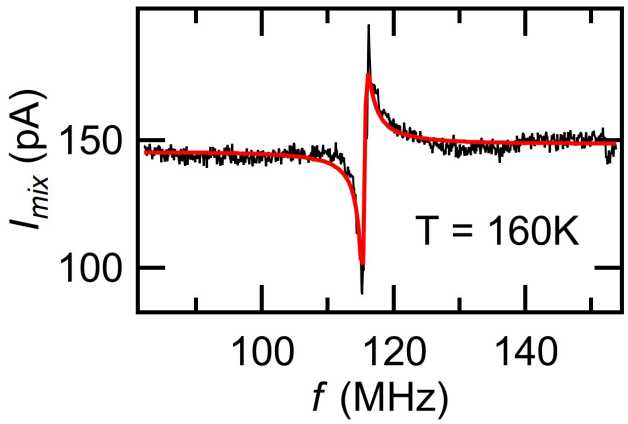

Figure 3.3: Electromechanical resonance in a bilayer graphene resonator at 160 K. The raw data is shown in black and the theoretical model is shown in red. A sharp, high frequency, high quality resonance in Device A can be seen at 160 K. Note that the fitting works even when the oscillation is completely out-of-phase and the Lorentzian lineshape is hard to distinguish. Above 160 K, our cryostat could not cryopump effectively and the sample got dirty. With a more reliable vacuum, it should be possible to measure bilayer graphene electromechanical resonances at room temperature. The data was taken at $V_G = -6\ V$, $\delta V_B = 5\ mV$, and $\delta V_G = 5\ mV$.

At the level of understanding described thus far, the resonance becomes a platform to explore the properties of the resonator, such as nonlinearity and morphology.

3.2 Duffing Nonlinearity in BG-NEMS

A driven damped harmonic oscillator obeys the equation $\ddot{z}+\frac{\omega_0}{Q}\dot{z}+\omega_0^2 = f(t)$. This equation is insufficient to explain oscillators whose behaviour changes qualitatively with varying drive power (nonlinear oscillators), which we observe in our resonators (see Figure 3.4).

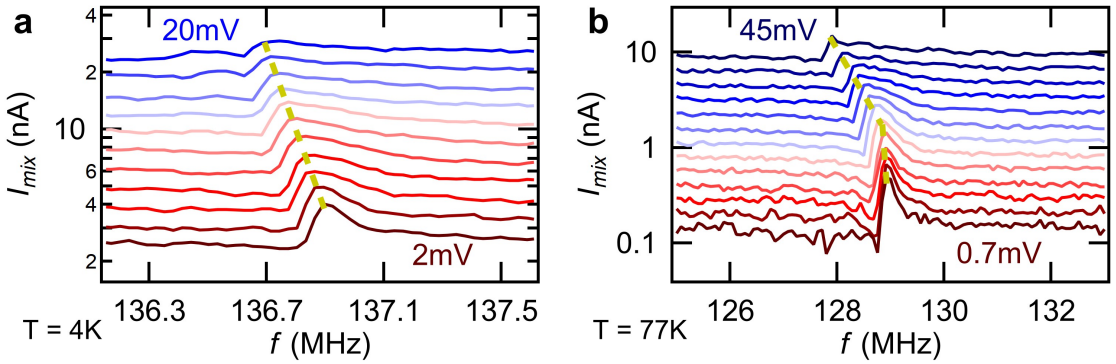

Figure 3.4: Nonlinear frequency softening in device A at 4 K and 77 K. The left axis indicates the mixing current measured. The bottom axis is the frequency of the sweeps. Colour scale is increasing drive voltage from red to blue. As drive force is increased, resonance frequency is decreased. The data at 4 K were taken at $V_G = 6\ V$ and $\delta V_S = 5\ mV$. The data at 77 K were taken at $V_G = -6\ V$ and $\delta V_S = 2.85\ mV$.

The simplest and most studied nonlinear restoring force is called Duffing nonlinearity (parameterized by the "Duffing parameter" α). This is also the most studied type of nonlinearity in graphene NEMS [14]. A Duffing oscillator is described by the equation [51]:

$$\ddot{z} + \frac{\omega_0}{Q}\dot{z} + \omega_0^2 z + \alpha z^3 = f(t) \tag{3.3}$$

Where z is the displacement from equilibrium, ω_0 is the resonance frequency, Q is the quality factor, and $f(t)$ is the sinusoidally varying forcing function. While this describes our system well enough to explain its behaviour in most regimes, Samanta et Al. [51] provide a full description of the geometric nonlinearity of an electromechanical

membrane oscillator. In this description, instead of only αz^3, terms of all orders $\sum_2^\infty \alpha_i z^i$ are included. At realistic values of strain and amplitude, most of these terms are suppressed so an effective Duffing parameter α_{eff} [6] is usually used. The dominant terms in the expression for α_{eff} are quadratic α_2 and cubic α_3.

$$\alpha_{eff} = \alpha_3 - \frac{10\alpha_2^2}{9\omega_0^2} \tag{3.4}$$

The geometry of a membrane resonator results in the following expressions for the quadratic and cubic nonlinearities [51]:

$$\alpha_2 = \frac{E\delta z_{dc}}{6\rho}\left(\frac{2\pi}{L}\right)^4 - \frac{5E\delta z_{dc}^3}{72\rho}\left(\frac{2\pi}{L}\right)^6 - \frac{5}{2}\sqrt{\frac{2}{3}}\frac{c_G^{(3)}}{\rho t}\left(V_G^{DC}\right)^2 \tag{3.5}$$

$$\alpha_3 = \frac{E}{18\rho}\left(\frac{2\pi}{L}\right)^4 - \frac{5E\delta z_{dc}^2}{72\rho}\left(\frac{2\pi}{L}\right)^6 - \frac{35}{9}\frac{c_G^{(4)}}{\rho t}\left(V_G^{DC}\right)^2 \tag{3.6}$$

Where E is the effective 3D Young's modulus, ρ is the density (we use the density of graphite in our calculations), t is the thickness, and $c_G^{(n)}$ is the n^{th} derivative of the capacitance per unit area with respect to the suspension height.

For weak nonlinearity, the Duffing parameter can be extracted from the frequency shift as amplitude is increased [52] (see Equation 3.7). This procedure is performed on our data in Figures 3.5 and 3.6.

$$\omega = \omega_0 + \frac{3}{8}\frac{\alpha}{\omega_0}\left(\delta z_0\right)^2 \tag{3.7}$$

BG-NEMSs have nonlinearity which turns on at low amplitude and can be seen in our samples as frequency shifting versus amplitude.

Based on the length and frequency of our oscillator, we calculate a Duffing

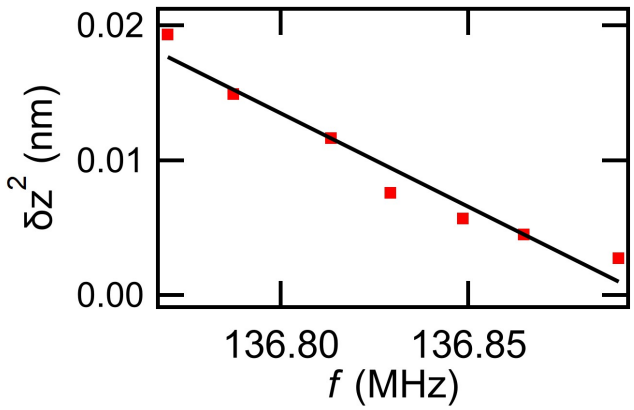

Figure 3.5: Extracting the Duffing parameter in device A at 4K.
From the data in panel *a* of Figure 3.4, we extract amplitude squared (right) and resonance frequency (left). The derivative is $\frac{\partial \delta z^2}{\partial f} = (-1.39 \pm 0.14) \times 10^{-25}\ m^2 s$. Using Equation 3.7, this corresponds to $\alpha_{eff} = -1.0 \times 10^{35}\ Hz^2/m^2$.

parameter with similar magnitude to our measurements (calculated $\alpha_{eff} = (2.6 \pm 0.2) \times 10^{34}\ Hz^2/m^2$ compared to our measured value $\alpha_{eff} = -1.0 \times 10^{35}\ Hz^2/m^2$). For this calculation, and throughout the thesis, we follow C. Chen [14] and assume an effective Young's modulus of 1 TPa. An effective Young's Modulus (3D) is reported instead of a 2D Young's Modulus in order to facilitate comparison between monolayer and bilayer graphene as well as to simplify some equations. There are several contradictory reports of this value in literature: 1 ± 0.2 TPa [53], 2 ± 0.5 TPa [54], and 594 ± 45 GPa [18], for example. We artificially exclude the error on this value from the reported uncertainties. The sign of our measured nonlinearity is opposite our expectations, suggesting that quadratic nonlinearity plays a larger role than anticipated (by Equation 3.4).

At higher amplitudes and higher temperature (more noise, less strain), two different regimes for nonlinearity can be identified (see Figure 3.6).

As discussed in Samanta et. Al. [51], bistable or even mutistable behaviour (which shows as jumps on the frequency sweep) can be present in the strongly nonlinear regime, which we also observe.

There is disagreement between our results and the mathematical predictions for

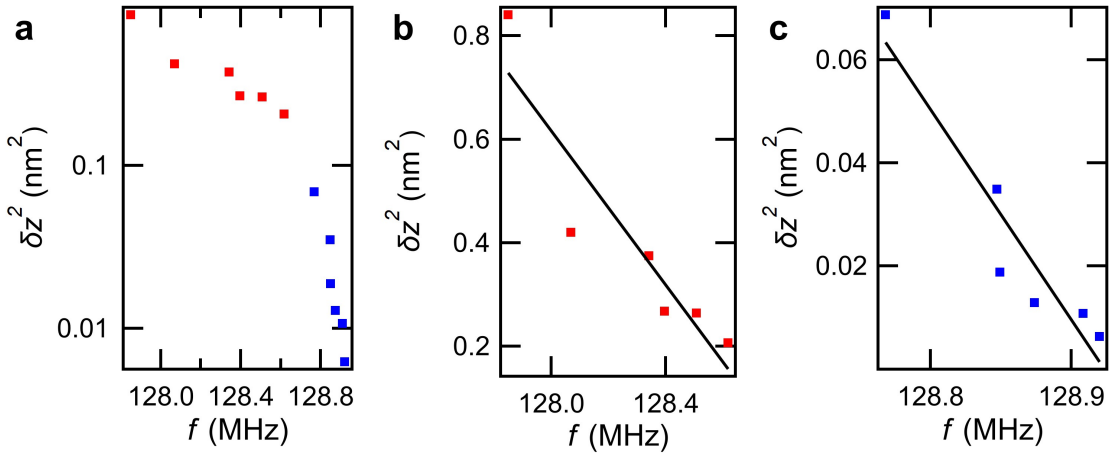

Figure 3.6: Extracting Duffing parameter in device A at 77K.
From the data in panel *b* of Figure 3.4 following the procedure from Figure 3.5. **a** Raw data at 77K, two regimes are identified in red and blue corresponding to the two regimes seen in panel *b* of Figure 3.4. **b** Fit of the high amplitude regime with a higher $\alpha_{eff} \approx 6\alpha^{(4K)}$. **c** Fit of the low amplitude regime with lower $\alpha_{eff} \approx 3\alpha^{(4K)}$.

the nonlinearity of a membrane resonator (and, as we shall see, the relationship between strain and frequency). We propose a simple picture in which changing morphology can cause these behaviours and present evidence that this picture is correct and represents an improvement in understanding BG-NEMS.

3.3 Tuning BG-NEMS through Wrinkles and Ripples

When a 2D resonator is subjected to an electric field, the capacitive forces affect its morphology. We show that our measurements are consistent with morphological wrinkling and rippling present in literature. The evidence which we found that supports this picture is:

1. Quadratic frequency hardening which is inconsistent with the quartic behaviour from the theory for membrane oscillators [14]. Refer to Figures 3.8 and 3.10.
2. A gap in the frequency of oscillation at a frequency where membrane behaviour begins to resemble the observed hardening [41]. Refer to Figure 3.11.

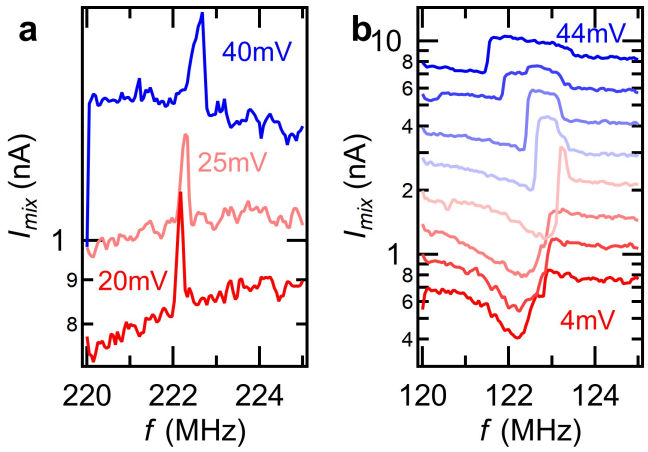

Figure 3.7: Multistable electromechanical resonance in device A and also in device B. Similar to the report by Samanta et Al. in monolayer graphene [51], we observe discontinuities in the frequency of oscillation. These discontinuities with a sample at different drive powers represent jumps between two stable oscillation amplitudes for a given frequency of oscillation. **a** Device B at $\approx 4\ K$, $V_G = 1.18\ V$, $\delta V_B = 10\ mV$. **b** Device A at $\approx 120\ K$, $V_G = -6\ V$ and $\delta V_B = 2.85\ mV$.

3. A gap size in quantitative agreement with nonlinear mode mixing between a mostly-flat mode shape and a spatially varying mode shape [19][55]. Refer to Equation 3.14.

4. An intra-band conductance minimum coincident with the mode mixing, as expected from morphological irregularity [56]. Refer to Figure 4.3.

5. Nonlinear damping which is not accounted for by the membrane model, and other nonlinearities corroborate this picture [57]. Refer to Figure 3.15.

The frequency of a membrane resonator can be tuned by varying the DC gate voltage. Since the device is a capacitor, charge from the gate builds up on either plate of the capacitor causing an attractive force and thereby inducing a tension and varying the frequency [14].

C. Chen et Al. demonstrated that modelling graphene NEMS as membrane resonators reproduces the qualitative behaviours that were observed [50]. On Page 71 of C. Chen's thesis [14], however, it is clear that this qualitative agreement does not fully capture the shape (quadratic hardening) which was measured for the NEMS

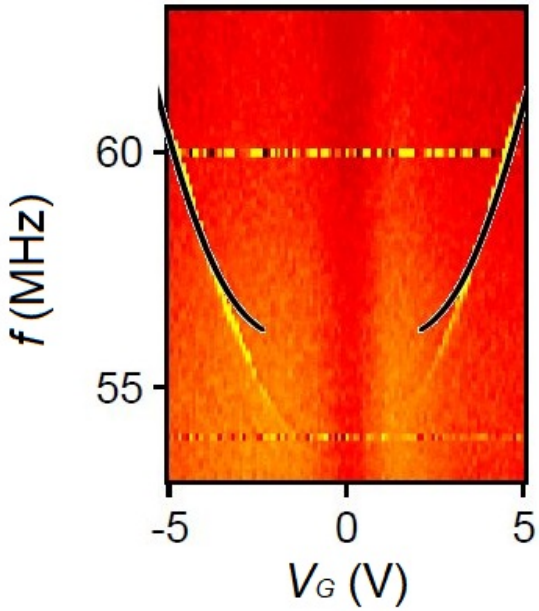

Figure 3.8: Disagreement between the quartic hardening of $f - V_G$ (as predicted for a membrane oscillator) and the data reported in literature.
When a gate voltage is applied to NEMS, it induces a tension which tunes the frequency. The fit from C. Chen's PhD thesis overlaid on the quadratic hardening behaviour actually presented in the same thesis [14]. The left axis is frequency and the bottom axis is gate voltage used to modulate the tension in the sample. The colour scale is mixing current and the black line is the fit to the frequency tuning data reported in the PhD thesis.

most similar to ours (see Figure 3.8).

3.4 Frequency, Strain, and Nonlinear Mode Mixing

The force stretching the membrane induces a tension described by the static displacement of the oscillator with an effective spring constant given by:

$$k = \left(\frac{16ELWt\varepsilon_0}{L^2} - \frac{c''LWtV_G^2}{2L}\right) + \frac{256ELWt}{9L^4}z^2 \tag{3.8}$$

Moreover, when net force is zero, $kz = \frac{c'WtV_G^2}{2}$. Since the frequency is given by

$f = \sqrt{\frac{k}{m_{eff}}}$, we can rearrange to get [14]:

$$\frac{f^2}{f_0^2} = \left(1 - \beta_0 V_G^2\right)\left(1 + \frac{1}{3}\left(\frac{R^2-1}{R}\right)^2\right) \tag{3.9}$$

Where $R = \left(\left(1 + \frac{\left(\gamma_0 V_G^2\right)^2}{\left(1-\beta_0 V_G^2\right)^3}\right)^{\frac{1}{2}} - \left(\frac{\left(\gamma_0 V_G^2\right)^2}{\left(1-\beta_0 V_G^2\right)^3}\right)^{\frac{1}{2}}\right)^{\frac{1}{3}}$, $\frac{c'' L^2}{32Et\varepsilon_0} = \beta_0$, and $\left(\frac{1}{\varepsilon_0}\right)^{\frac{3}{2}} \frac{9c'L}{16Et} = \gamma_0$. ε_0 is the built-in strain and C', C'' are the first and second derivatives of the gate capacitance. The resonance frequency at zero gate is $f_0^2 = \frac{16E\varepsilon_0}{\rho L^2}$ and finally $\gamma_0 = \frac{9c'L}{16Et\varepsilon_0}\varepsilon_0^{-\frac{1}{2}}$, $\beta_0 = \frac{3c''L^2}{32Et\varepsilon_0}$. Extracting f_0 and V_{CNP} from the bottom of the curve reduces the problem to a two-parameter fit for the frequency tuning (demonstrated in the red fit in Figure 3.10).

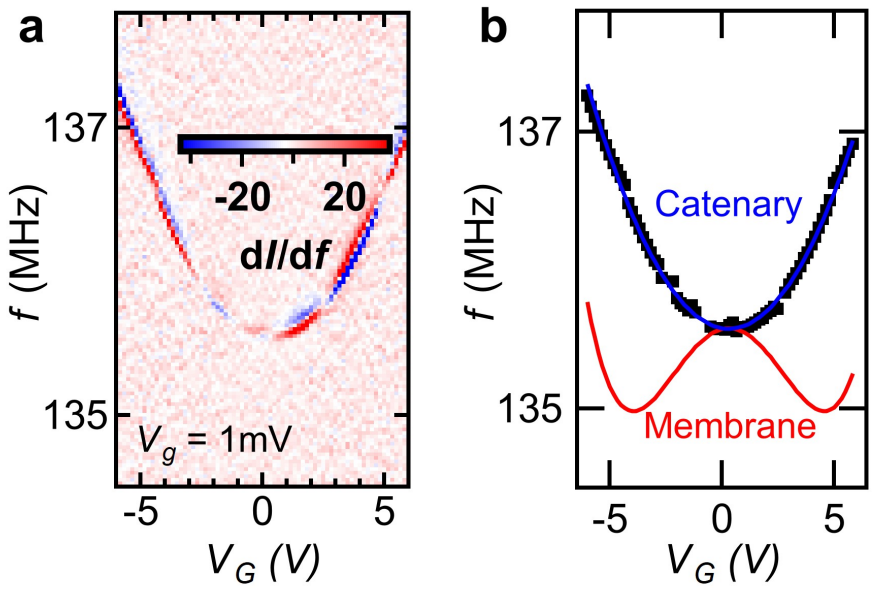

Figure 3.9: Comparison between catenary and membrane tuning in device A. Left axis is frequency, bottom axis is gate voltage. **a** Raw 2D $f - V_G$ mixing data. Colour scale is the rate of variation of current versus frequency (chosen to achieve a uniform background and good visibility of resonance tuning). Taken at $\approx 4\ K$, $\delta V_S = 2\ mV$ and $\delta V_G = 1\ mV$. **b** Extracted data and predicted frequency hardening for a membrane (red, using Equation 3.9) and a catenary beam (blue, using Equation 3.10). Surprisingly, the catenary physics is in much better agreement. The fitted values are given in Equation 3.11.

V. Sazonova et Al. give a different mechanism for frequency tuning [41], albeit in carbon nanotube NEMS. In the so-called "catenary" regime, the frequency of a system under slack changes primarily due to morphology as opposed to strain (demonstrated in the blue fit in Figure 3.10).

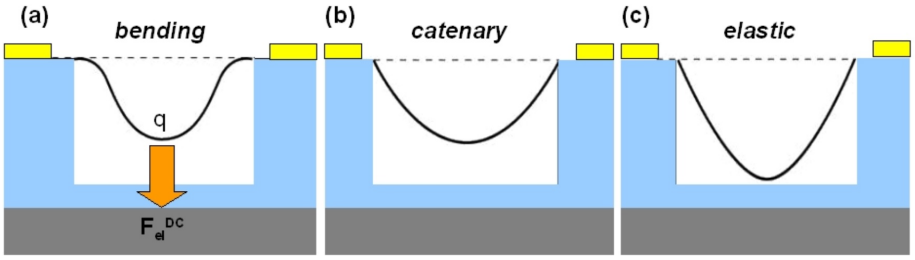

Figure 3.10: A cartoon of the catenary regime.
There are three regimes for a beam-like oscillator. The first (least strain) regime is the bending regime governed by the stiffness of the oscillator; in this regime the frequency is constant. The next (intermediate strain) regime is the catenary regime governed by changes in shape but not length; in this regime, quadratic tuning is expected. The final regime is the strained regime governed by strain $\frac{\Delta L}{L}$; in this regime, we expect the membrane description to be mostly valid. This figure was reproduced from the thesis by V. Sazonova [58].

$$\omega^{cat} = \frac{22.4}{L^2}\sqrt{\frac{Et^2}{12\rho}} + 0.28\frac{Lc'_G}{t^2\sqrt{8s}}\sqrt{\frac{1}{\rho E}}\left(V_G^{DC}\right)^2 \tag{3.10}$$

The above equation should be valid for a beam-like oscillator between $V_G = \sqrt{\frac{Et^3}{Lc'_G}\sqrt{\frac{2s}{3}}}$ and below $V_G = \sqrt{\frac{2\left(\frac{27}{25}\right)^{\frac{3}{2}} Ets^{\frac{3}{2}}}{Lc'_G}}$ [41].

Surprisingly, this quadratic hardening is a much better fit for the data in our device A as well (as shown in Figure 3.10). It describes a beam resonator with some slack so that changes in frequency are due to changes in geometry, not tension. In our device A, we find excellent agreement with the fit:

$$f = (135.38 \pm 0.01\ MHz) + \left(44.5 \pm 0.4\ \frac{kHz}{V^2}\right)(V - (0.30 \pm 0.01\ V))^2 \tag{3.11}$$

Under what condition can we expect a BG-NEMS oscillator to obey the catenary equation for a beam oscillator? In terms of the displacement from equilibrium (δz^{DC}), the equation for frequency of a membrane oscillator is (by rearranging Equation 3.8):

$$\omega = \sqrt{\frac{k\left(V_G\right) + \frac{32ELWt}{9L^4} z^2\left(V_G\right)}{m_{eff}}} \tag{3.12}$$

Suspended 2D materials in literature have been observed to exhibit "wrinkling" [43]. Suppose the "built-in" strain of the wrinkles were greater than the strain from the gate. By Equation 3.12, this corresponds to an RMS height of $z > \left(\left(\frac{2\pi}{22.4}\right)^2 \frac{\rho f_0^2 L^4}{E}\right)^{\frac{1}{3}} \approx 10\ nm$, similar to the wrinkles reported in literature [43].

In this scenario, the wrinkles would contribute an amount of virtual "slack" $s = \frac{0.28^2}{96} \frac{{c'_g}^2 L^2}{\left(2\pi \frac{df}{dV^2}\right)^2 E t^4} \approx 10^{-4}$ for which a catenary beam model would represent the dynamics (changing shape without changing tension). Since the catenary model is expected to represent the dynamics of such a system above $V_G \approx \sqrt{\frac{Et^2\sqrt{s}}{L^3 c'_g}} \approx 1V$ (from Equation 3.10) [58], it is consistent that it should describe our samples.

In the catenary picture, we would also expect a crossover to membrane physics once the static strain is greater than the built-in strain of the wrinkles. From Equation 3.12, the unwrinkling regime is $k_0 \approx \frac{32ELWt}{9L^4} z_{RMS}^2$, which would correspond to $f_0 > \frac{8 z_{RMS}}{3L^2} \sqrt{\frac{E}{\rho_{eff}}}$ or approximately 100 MHz.

Moreover, when two different modes are excited simultaneously (ex: degeneracy, pumping, or harmonics) they couple through the Duffing nonlinearity (discussion by Mathew et. al. [55]) according to the following equations:

$$\begin{aligned} \ddot{z_1} + 2\zeta \dot{z_1} + \omega_1^2 z_1 + \alpha_1 z_1^3 + \alpha_{12} z_2^2 z_1 &= f_1\left(t\right) \\ \ddot{z_2} + 2\zeta \dot{z_2} + \omega_2^2 z_2 + \alpha_2 z_2^3 + \alpha_{12} z_1^2 z_2 &= f_2\left(t\right) \end{aligned} \tag{3.13}$$

Where $\alpha_i = \alpha \left(\int dz {\phi'_i}^2\right)^2$ and $\alpha_{12} = \alpha \left(\int dz {\phi'_1}^2\right)\left(\int dz {\phi'_2}^2\right)$. The subscripts 1 and 2 denote the two modes which are coupling to one another. The Duffing parameter

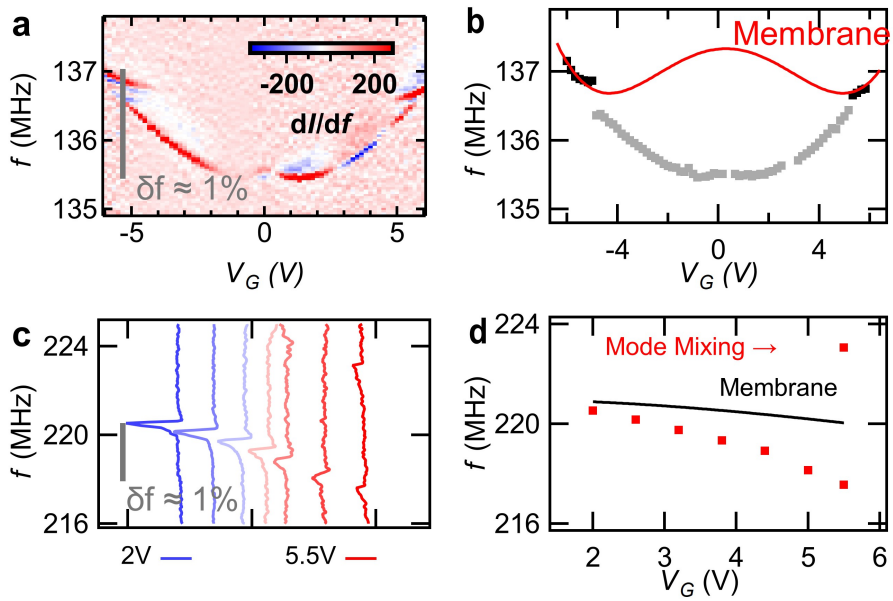

Figure 3.11: Presence of frequency gap in devices A and B.
At high power, we observe a gap in the frequency. **a** Frequency tuning in Device A at 4.2 K at $\delta V_s = 5\ mV$ and $\delta V_g = 10\ mV$. **c** Frequency tuning in Device B at 4.2 K at $\delta V_S = 10\ mV$ and $\delta V_G = 10\ mV$. From Equation 3.14, **b** $\alpha_{12} = 6.9 \times 10^{33}\ Hz^2/m^2$ for device A and **d** $\alpha_{12} = 3.3 \times 10^{36}\ Hz^2/m^2$ for device B. Both differ by a factor of 100 (in opposite directions) from the measured Duffing parameter. This is consistent with coupling to modes with dramatically different mode shapes $\int dz {\phi_2'}^2$ such as between wrinkled and membrane oscillations.

α is involved via the α_{12}, which also contains a term related to the mode shape.

When the two modes couple strongly, a gap in the frequency appears (also known as an avoided crossing). We observe avoided crossings in both our devices at high power (see Figure 3.11).

$$\Delta_\omega = \left(\sqrt{\omega_1^2 + \alpha_{12} \frac{\delta z_2^2}{2}} \right) - \omega_1 \tag{3.14}$$

The strength of the mode coupling is usually given by the cooperativity C [59], a dimensionless factor which is used to report device performance:

$$C = \frac{Q_1 Q_2}{\omega_1 \omega_2} \Delta_\omega^2 \tag{3.15}$$

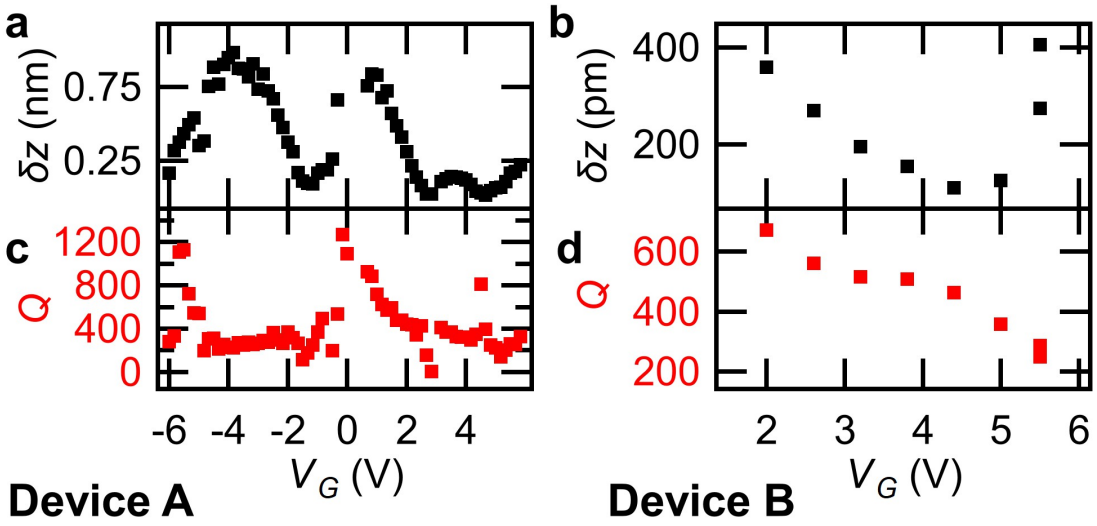

Figure 3.12: Gate-tunable δz showing impact of avoided crossings on Q. Highly tunable amplitude and quality factor at high drive in device A at 4K. **a** and **c** correspond to the data in panel a of Figure 3.11 at $\delta V_S = 5\ mV$ and $\delta V_G = 10\ mV$. **b** and **d** correspond to the data in panel b of Figure 3.11 at $\delta V_S = 10\ mV$ and $\delta V_G = 10\ mV$.

From the α_{12}'s in Figure 3.11, we extract cooperativity $C \approx 4$ for device A and $C \approx 36$ for device B using Equation 3.15.

In Figure 3.12, we can see highly tunable amplitude at constant power. While this is an interesting applied property by itself, it also accounts for the large difference in gap size for holes and electrons in Figure 3.11 (from Equation 3.14). Furthermore, in Figure 3.13 we can see the phase of the oscillator is negative on either side of the gap, showing strong leakage of mechanical energy.

Our mode mixing measurement permits indirect detection of mode shape variation. Accordingly, we suggest that further study on electronic effects of dynamical chaos in BG-NEMS is a promising and near-term aim in the understanding of 2D NEMS, particularly for the relationship between their nonlinearity and morphology.

Suppression of the conductivity as charge density increases is observed coincident to the frequency gap (see Figure 4.3). This is consistent with our picture since

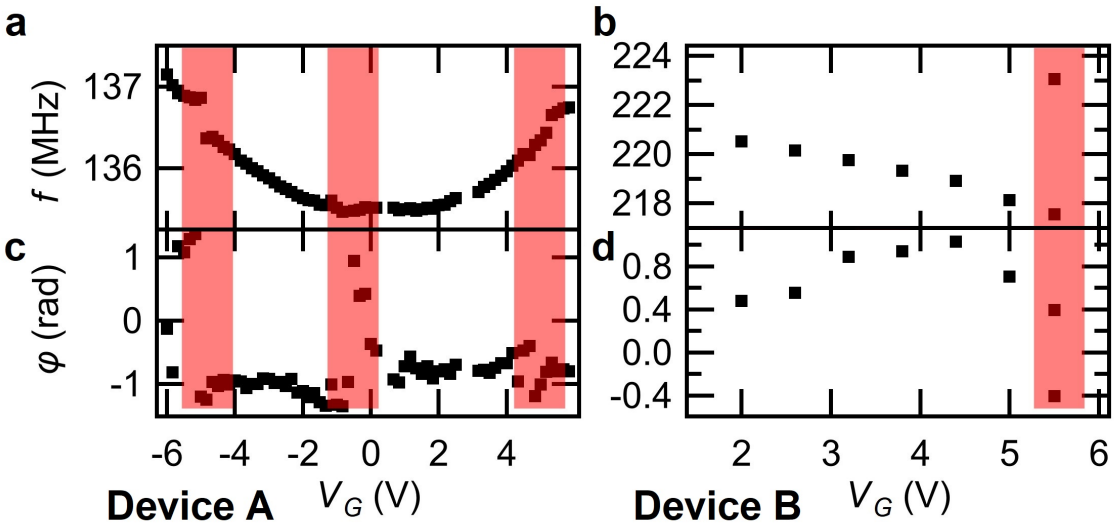

Figure 3.13: Effects of mixed mode on oscillator phase above and below avoided crossings.
The phase (**c**,**d**) of the resonance on either side of the discontinuity (**a**,**b**) has opposite sign. The data are taken at the same parameters as in Figure 3.11.

surface disorder can be related to an effective suppression of the mean free path (and therefore mobility). The fractal ripples of graphene are well-studied [60] and the relationship between the wrinkle fractal dimension and the suppression of mobility is known theoretically [56]. In particular, the excess resistivity $\delta\rho$ for highly fractal graphene is given by Equation 3.16.

$$\delta\rho = \frac{h}{4e^2}\frac{\tilde{z}^4}{\tilde{R}^2 a^2} \tag{3.16}$$

Where h is Planck's constant, $\tilde{z}$ is the characteristic height of the ripples, $\tilde{R}$ is the characteristic radius of the ripples, and a is the lattice constant.

As a membrane geometry fails to account for the magnitude of the nonlinearity, the morphological change provides a unified mechanism that can explain the effects observed in this section.

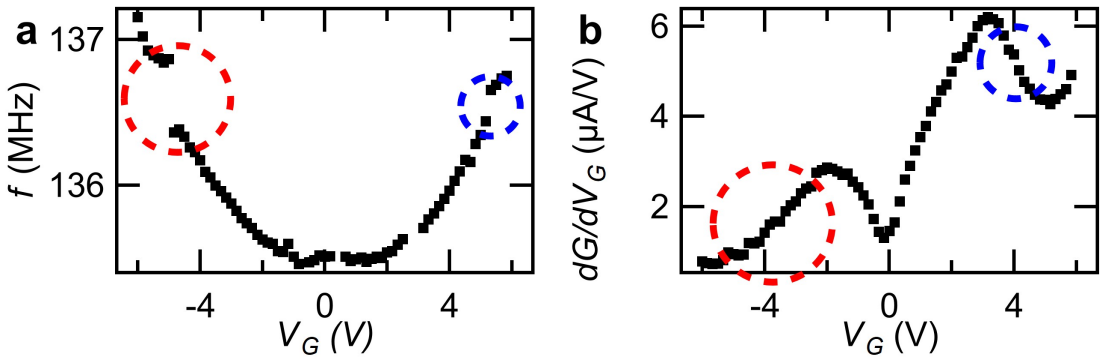

Figure 3.14: Impact of RF NEMS mode mixing on DC charge conductivity. **a** Morphological mode mixing in Device A. **b** Intra-band conductance minimum corresponding to suppression of mobility. The excess resistance at the frequency gap can be described by large morphological disorder via Equation 3.16. The data are taken at the same parameters as in Figure 3.11.

3.4.1 Nonlinear Damping in BG-NEMS

A second form of nonlinearity has been reported in graphene NEMS and is called nonlinear damping [57][20]. Nonlinear damping is described by the parameter η in Equation 3.17.

$$\ddot{z} + \frac{\omega_0}{Q}\dot{z} + \omega^2 z + \eta z^2 \dot{z} + \alpha z^3 = f(t) \tag{3.17}$$

When the frequency shift due to Duffing nonlinearity is on the order of the linewidth broadening due to nonlinear damping, the linewidth changes proportionally to the frequency shift grows proportionally to one another, according to the relationship in Equation 3.18 [57]:

$$Q_{\delta z}^{-1} = 2\frac{\eta}{\alpha}(\omega - \omega_0) + Q^{-1} \tag{3.18}$$

Although nonlinear damping is not expected for a system that behaves strictly like a membrane resonator [57], we observe nonlinear damping in our BG-NEMS as

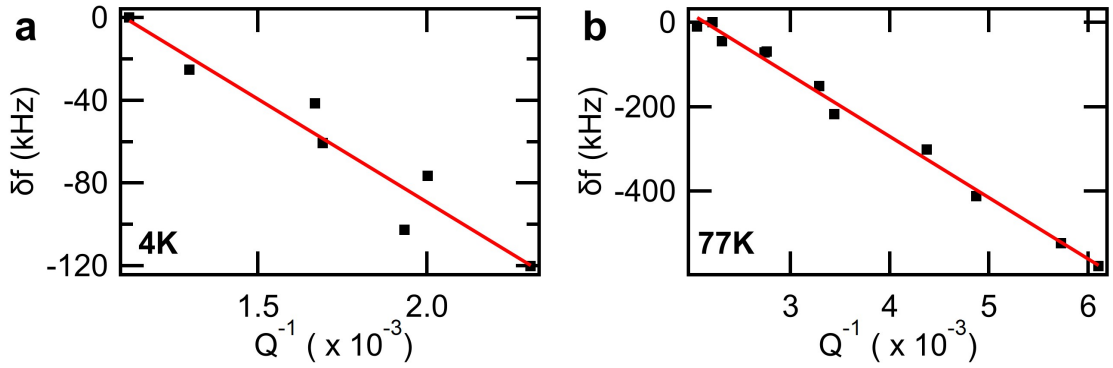

Figure 3.15: Extracting η from amplitude dependence of Q.
Nonlinear damping can be seen from a linear relationship between the frequency shift and the broadening in device A at 4 K and 77 K.. At 4K $\frac{\partial Q^{-1}}{\partial f} = -3.841\ ns$ corresponding to $\eta = 5.0 \times 10^{27}\ Hz/m^2$

a resonance broadening with increased drive force (subtle, but visible effect in Figure 3.4). We plot the frequency shift versus the resonance broadening in Figure 3.15. Using Equation 3.18, we obtain a value of $\eta \approx 5.0 \times 10^{27}\ Hz/m^2$ at 4K and a value of $\eta \approx 9.4 \times 10^{27}\ Hz/m^2$ at 77K.

Nonlinear damping has been observed in literature with a magnitude greater than can be explained by a membrane geometry alone [57][20]. In our devices, we also observe nonlinear resonance broadening which is linear in frequency shift (see Figure 3.15). This is consistent with nonlinear damping.

Our observation of suppressed mobility in Figure 4.3 of the preceding section provides a possible mechanism of action for nonlinear energy loss through nonlinear mode coupling to modes associated with the wrinkled morphology.

3.5 Summary of our Results: Tunable, Nonlinear, Wrinkled BG-NEMS

We demonstrated the clear detection of high-quality and tunable electromechanical resonances in two BG-NEMS. The properties of our resonators are summarized in Table 3.1.

Device	A	B
$L\ (\mu m)$	1.07	1.64
$W\ (\mu m)$	1.21	0.29
$\mu\ (\frac{cm}{Vs})$	76 000	57 000
$f\ (MHz)$	137	216
$\delta z^{max}\ (nm)$	0.5	0.1
$\alpha_2\ (Hz^2/m)$	4.4 $\times 10^{25}$	1.6 $\times 10^{24}$
$\alpha_3\ (Hz^2/m^2)$	2.9 $\times 10^{34}$	5.3 $\times 10^{33}$
$\alpha^{(calc)}\ (Hz^2/m^2)$	2.6 $\times 10^{34}$	5.3 $\times 10^{33}$
$\alpha^{(meas)}\ (Hz^2/m^2)$	-1.0 $\times 10^{35}$	
$\eta\ (Hz/m^2)$	5.0 $\times 10^{25}$	
$\lvert\alpha_{\mu\nu}\rvert\ (Hz^2/m^2)$	6.9 $\times 10^{33}$	3.3 $\times 10^{36}$
C	4.2	36

Table 3.1: Summary of the NEMS properties of devices A and B at 4K. Nominal values for the following quantities: length, width, mobility, frequency, max amplitude. Calculated values for: quadratic and cubic nonlinearity. Measured values for: effective Duffing parameter and nonlinear damping as well as nonlinear mode coupling and cooperativity. A discussion of the uncertainty is made in the body of the text.

Using the gate voltage, we were able to tune the frequency of both of our devices by 1%. We were able to observe these resonances at temperatures up to 160 K. By varying the morphology via the gate voltage, we were able to tune the quality factor by 400% and the resonance amplitude by 700%. For a change in strain on the order of 1%, we see a qualitative change in the $f - V_G$ dispersion. By comparing the measured $f - V_G$ dispersion to expectations for both a membrane and a catenary oscillator, and by comparing our measured α's to our measured α_{12}'s, we explain the behaviour of our devices in terms morphological wrinkles and ripples.

Chapter 4

Conclusions

In this thesis, we have contributed three clear advancements to the study of 2D NEMS. Firstly, we have presented a mixing detection of electromechanical resonance in BG-NEMS. Next, we have demonstrated gate-controlled tuning of the frequency and quality factor of these resonators. Lastly, we have examined how nonlinearity of the BG-NEMS is related to tunable morphological features.

4.1 Electromechanical Actuation and Detection of Bilayer Graphene NEMS Resonance

To the best of our knowledge, electromechanical activation of BG-NEMS, measurement of their mobilities, and detection of their electromechanical resonances has not been explicitly reported. We fine-tune methods from literature to fabricate BG-NEMS of high quality, anneal BG-NEMS to low-disorder, and measure BG-NEMS at their driven resonances with minimal circuit artefacts.

This simultaneous actuation and detection allowed us to report two BG-NEMS resonators (example in 4.1) with frequencies $f \approx 137$ MHz and $f \approx 220$ MHz, at mobilities up to $\mu \approx 76000\ cm^2/Vs$, with quality factors as high as $Q \approx 2000$, at temperatures as high as 160 K.

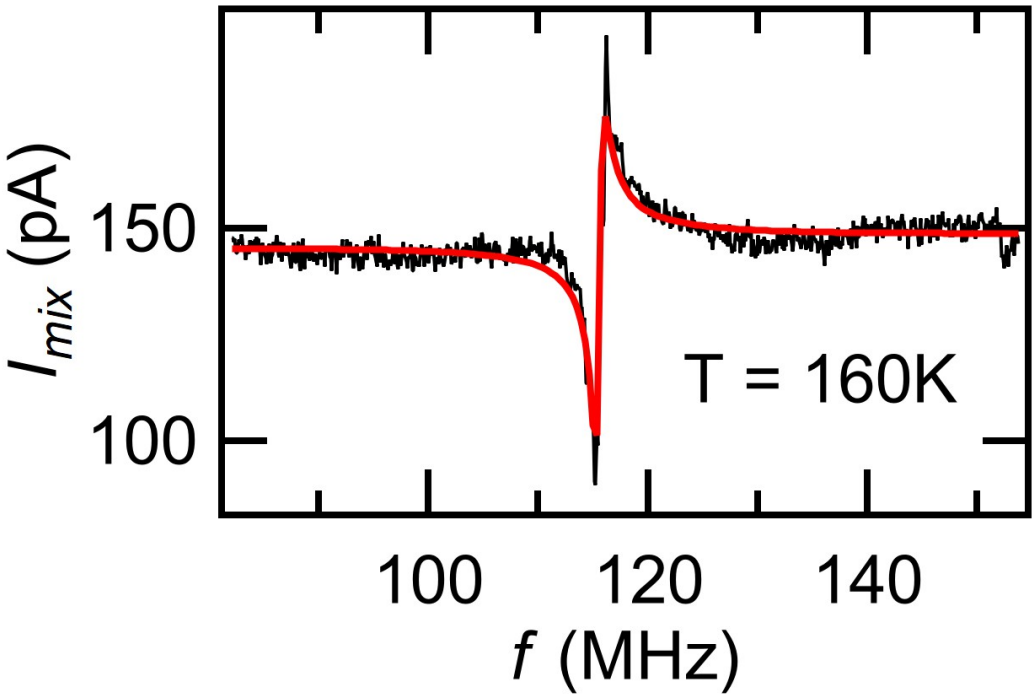

Figure 4.1: Mixing current detection of electromechanically actuated BG-NEMS.

Given our results, we expect that small modifications to the cryostat vacuum system will permit room-temperature measurements of BG-NEMS. Moreover, we expect our techniques to extend to novel carbon 2D materials like twisted bilayer graphene and ABC-stacked trilayer graphene.

4.2 NEMS with Tunable f Near the Charge Neutrality Point: Study of Low-Energy 2D Physics

The BG-NEMS we report are tunable with an applied gate voltage. The gate voltage controls charge density and the strain, allowing the resonance frequency to be tuned.

Using the gate voltage, the resonance frequencies of our BG-NEMS can be tuned

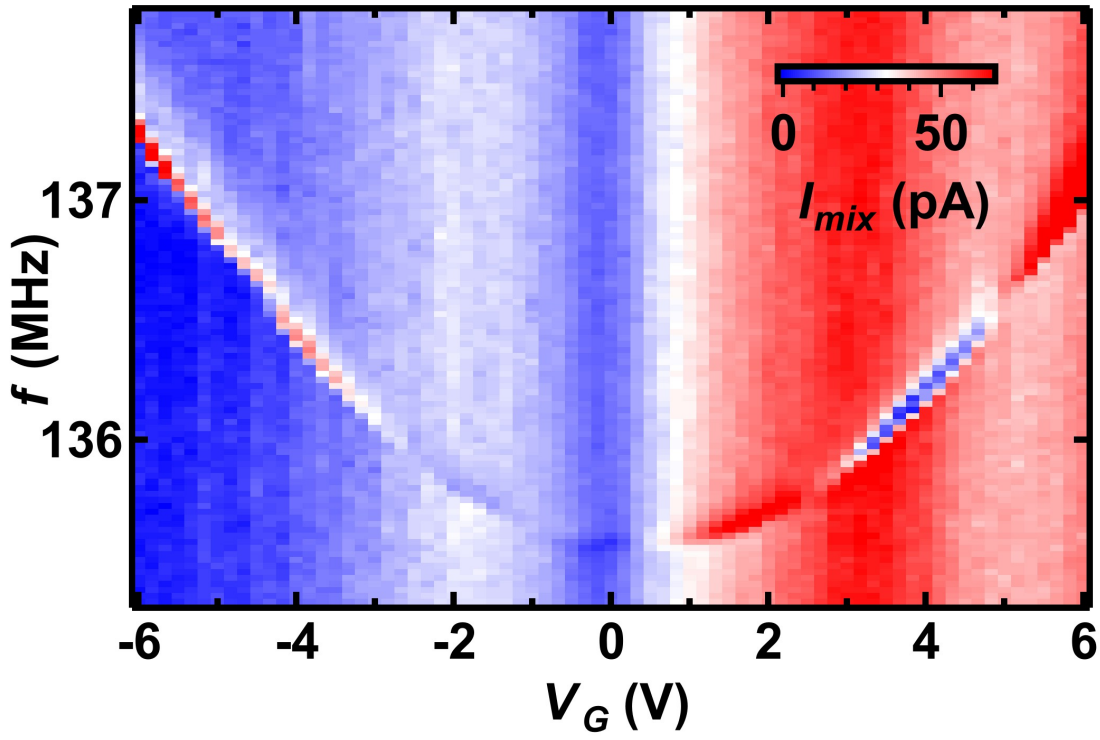

Figure 4.2: Raw $f - V_G$ mixing current data clearly showing resolution of CNP.

by $\approx \pm 1\%$. Moreover, we report good resolution of the charge neutrality point (see Figure 4.2): we detect resonances at charge densities as low as $n < 6.6 \times 10^{-9}\ cm^{-2}$).

With tunable resonance frequency, good resolution of the low-energy physics, and detection at temperatures as low as $50mK$, we expect to be able to mechanically detect low-energy excitations in BG-NEMS and related systems, such as the quantum Hall effect states, proximity-induced superconductivity, quantum dots, and correlated electrons.

4.3 Morphologically Tunable Nonlinearity in BG-NEMS

By varying the drive power of the BG-NEMS, we measured nonlinear behaviour including hardening, softening, broadening, and multistability. The properties of our

nonlinear oscillators depended strongly on strain and temperature and allowed us to propose a relationship with the morphology.

When as the gate voltage approaches critical values, a large increase in the amplitude (up to 4000%) and the quality factor (up to 550%) were observed. Even when not on resonance, the differential mobility became negative at these values. At higher drive powers, these critical values also corresponded to gaps in the frequency of oscillation ($\Delta_f \approx 500$ kHz and $\Delta_f \approx 6$ MHz), corresponding to mode mixing with high cooperativity ($C \approx 4.2$ and $C \approx 36$). Warming up, evidence of higher-order nonlinearity with hardening, softening, and as many as 3 quasi-stable amplitudes was seen.

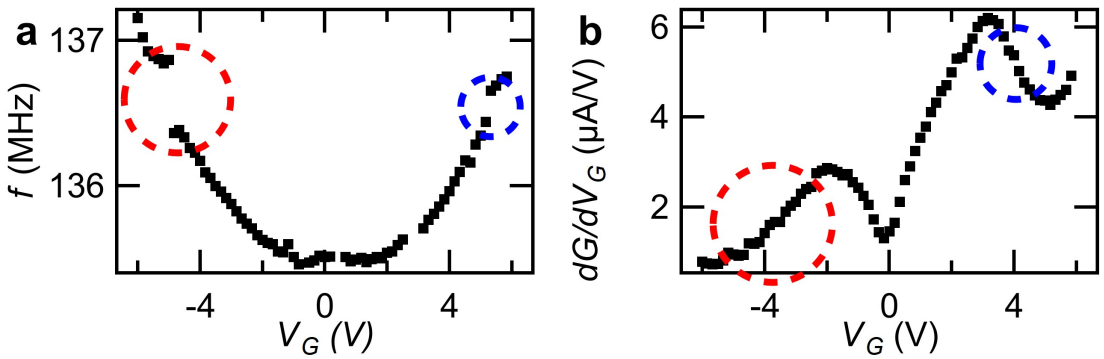

Figure 4.3: Morphological suppression of mobility.

While the evidence presented is consistent with literature in graphene monolayer NEMS experiment, it is not consistent with the accepted description of 2D NEMS as a membrane oscillators. We propose that 2D-NEMS morphology is tunable from 2D and membrane-like because of high strain to 3D and beam-like because of wrinkles from cooling and annealing.

4.4 Future Study: Pushing the Boundaries of Bilayer Graphene NEMS

We demonstrate bilayer graphene NEMS (example in Figure 4.4) with unique advantages such as the resolution of mixing current near the charge neutrality point. With the methods and devices described in this thesis, several avenues of future study can be identified.

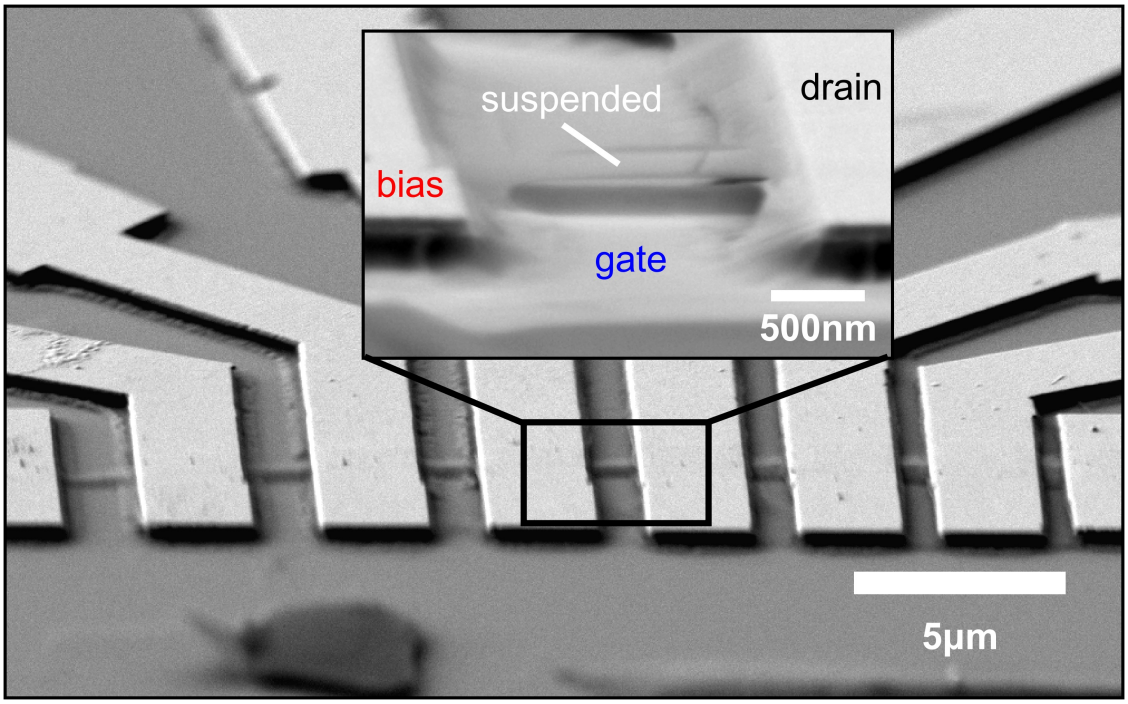

Figure 4.4: SEM image of our BG-NEMS.

An immediate objective is to measure at room temperature and above. Given our ability to resolve the resonance at 160 Kelvin, this is a realistic goal. In addition to exploring realistic device applications, access to room-temperature BG-NEMS would permit electromechanical measurement of graphene's thermal expansion.

Given the recent excitement surrounding twisted bilayer, the realization of this measurement in BG-NEMS opens up the possibility of studying the correlated electrons in magic-angle twisted bilayer graphene.

Bibliography

[1] G. Lammel. The future of mems sensors in our connected world. In *2015 28th IEEE International Conference on Micro Electro Mechanical Systems (MEMS)*, pages 61–64.

[2] W. M. Zhang, K. M. Hu, Z. K. Peng, and G. Meng. Tunable micro- and nanomechanical resonators. *Sensors (Basel)*, 15(10):26478–566, 2015.

[3] R. N. Patel, J. P. Mathew, A. Borah, and M. M. Deshmukh. Low tension graphene drums for electromechanical pressure sensing. *2D Materials*, 3(1):011003, 2016.

[4] K. L. Ekinci, Y. T. Yang, and M. L. Roukes. Ultimate limits to inertial mass sensing based upon nanoelectromechanical systems. *Journal of Applied Physics*, 95(5):2682–2689, 2004.

[5] V. Singh, S. Sengupta, H. S. Solanki, R. Dhall, A. Allain, S. Dhara, P. Pant, and M. M. Deshmukh. Probing thermal expansion of graphene and modal dispersion at low-temperature using graphene nanoelectromechanical systems resonators. *Nanotechnology*, 21(16):165204, 2010.

[6] G. J. Verbiest, J. N. Kirchhof, J. Sonntag, M. Goldsche, T. Khodkov, and C. Stampfer. Detecting ultrasound vibrations with graphene resonators. *Nano Letters*, 18(8):5132–5137, 2018.

[7] V. Singh, B. Irfan, G. Subramanian, H. S. Solanki, S. Sengupta, S. Dubey, A. Kumar, S. Ramakrishnan, and M. M. Deshmukh. Coupling between quantum

hall state and electromechanics in suspended graphene resonator. *Applied Physics Letters*, 100(23):233103, 2012.

[8] M. M. Benameur, F. Gargiulo, S. Manzeli, G. Autes, M. Tosun, O. V. Yazyev, and A. Kis. Electromechanical oscillations in bilayer graphene. *Nature Communications*, 6:8582, 2015.

[9] V. Singh, S. J. Bosman, B. H. Schneider, Y. M. Blanter, A. Castellanos-Gomez, and G. A. Steele. Optomechanical coupling between a multilayer graphene mechanical resonator and a superconducting microwave cavity. *Nature Nanotechnology*, 9:820, 2014.

[10] A. H. Castro Neto, F. Guinea, N. M. R. Peres, K. S. Novoselov, and A. K. Geim. The electronic properties of graphene. *Reviews of Modern Physics*, 81(1):109–162, 2009.

[11] X. Li, L. Tao, Z. Chen, H. Fang, X. Li, X. Wang, J.-B. Xu, and H. Zhu. Graphene and related two-dimensional materials: Structure-property relationships for electronics and optoelectronics. *Applied Physics Reviews*, 4(2):021306, 2017.

[12] C. Chen, S. Rosenblatt, K. I. Bolotin, W. Kalb, P. Kim, I. Kymissis, H. L. Stormer, T. F. Heinz, and J. Hone. Performance of monolayer graphene nanomechanical resonators with electrical readout. *Nature Nanotechnology*, 4(12):861–7, 2009.

[13] X. Song, M. Oksanen, M. A. Sillanpaa, H. G. Craighead, J. M. Parpia, and P. J. Hakonen. Stamp transferred suspended graphene mechanical resonators for radio frequency electrical readout. *Nano Letters*, 12(1):198–202, 2012.

[14] C. Chen. *Graphene NanoElectroMechanical Resonators and Oscillators*. PhD thesis, Columbia University, 2013.

[15] M. Huang, T. A. Pascal, H. Kim, W. A. Goddard, and J. R. Greer. Electronic–mechanical coupling in graphene from in situ nanoindentation experiments and multiscale atomistic simulations. *Nano Letters*, 11(3):1241–6, 2011.

[16] O. Shevchuk, V. Singh, G. A. Steele, and Y. M. Blanter. Optomechanical response of a nonlinear mechanical resonator. *Physical Review B*, 92(19), 2015.

[17] L. G. Villanueva, R. B. Karabalin, M. H. Matheny, E. Kenig, M. C. Cross, and M. L. Roukes. A nanoscale parametric feedback oscillator. *Nano Letters*, 11(11):5054–9, 2011.

[18] D. Davidovikj, F. Alijani, S. J. Cartamil-Bueno, H. S. J. van der Zant, M. Amabili, and P. G. Steeneken. Nonlinear dynamic characterization of two-dimensional materials. *Nature Communications*, 8(1):1253, 2017.

[19] M. H. Matheny, L. G. Villanueva, R. B. Karabalin, J. E. Sader, and M. L. Roukes. Nonlinear mode-coupling in nanomechanical systems. *Nano Letters*, 13(4):1622–6, 2013.

[20] V. Singh, O. Shevchuk, Y. M. Blanter, and G. A. Steele. Negative nonlinear damping of a multilayer graphene mechanical resonator. *Physical Review B*, 93(24), 2016.

[21] J. P. Mathew, R. N. Patel, A. Borah, R. Vijay, and M. M. Deshmukh. Dynamical strong coupling and parametric amplification of mechanical modes of graphene drums. *Nature Nanotechnology*, 11:747, 2016.

[22] K. S. Novoselov, A. K. Geim, S. V. Morozov, D. Jiang, Y. Zhang, S. V. Dubonos, I. V. Grigorieva, and A. A. Firsov. Electric field effect in atomically thin carbon films. *Science*, 306(5696):666–669, 2004.

[23] Z. Lin, A. McCreary, N. Briggs, S. Subramanian, K. Zhang, Y. Sun, X. Li, N. J. Borys, H. Yuan, S. K. Fullerton-Shirey, A. Chernikov, H. Zhao, S. McDonnell, A. M. Lindenberg, K. Xiao, B. J. LeRoy, M. Drndić, J. C. M. Hwang, J. Park, Ma.

Chhowalla, R. E. Schaak, A. Javey, M. C. Hersam, J. Robinson, and M. Terrones. 2d materials advances: from large scale synthesis and controlled heterostructures to improved characterization techniques, defects and applications. *2D Materials*, 3(4):042001, 2016.

[24] Y. Zhang, T. T. Tang, C. Girit, Z. Hao, M. C. Martin, A. Zettl, M. F. Crommie, Y. R. Shen, and F. Wang. Direct observation of a widely tunable bandgap in bilayer graphene. *Nature*, 459(7248):820–3, 2009.

[25] E. Yamaka and T. Sugita. Energy band structure in silicon crystal. *Physical Review*, 90(5):992–992, 1953.

[26] J. B. Oostinga, H. B. Heersche, X. Liu, A. F. Morpurgo, and L. M. Vandersypen. Gate-induced insulating state in bilayer graphene devices. *Nat Mater*, 7(2):151–7, 2008.

[27] E. V. Castro, K. S. Novoselov, S. V. Morozov, N. M. Peres, J. M. dos Santos, J. Nilsson, F. Guinea, A. K. Geim, and A. H. Neto. Biased bilayer graphene: semiconductor with a gap tunable by the electric field effect. *Physical Review Letters*, 99(21):216802, 2007.

[28] Y. Cao, V. Fatemi, A. Demir, S. Fang, S. L. Tomarken, J. Y. Luo, J. D. Sanchez-Yamagishi, K. Watanabe, T. Taniguchi, E. Kaxiras, R. C. Ashoori, and P. Jarillo-Herrero. Correlated insulator behaviour at half-filling in magic-angle graphene superlattices. *Nature*, 556(7699):80–84, 2018.

[29] Y. Cao, V. Fatemi, S. Fang, K. Watanabe, T. Taniguchi, E. Kaxiras, and P. Jarillo-Herrero. Unconventional superconductivity in magic-angle graphene superlattices. *Nature*, 556(7699):43–50, 2018.

[30] D. K. Ki, V. I. Fal'ko, D. A. Abanin, and A. F. Morpurgo. Observation of even denominator fractional quantum hall effect in suspended bilayer graphene. *Nano Letters*, 14(4):2135–9, 2014.

[31] A. J. Leggett. Lecture 5: Graphene electronic band structure and dirac fermions. https://uwaterloo.ca/institute-for-quantum-computing/sites/ca.institute-for-quantum-computing/files/uploads/files/lecture-5.pdf, June 2010. University of Waterloo. Phys 769: Selected Topics in Condensed Matter Physics. Accessed June 21st, 2019.

[32] E. McCann and M. Koshino. The electronic properties of bilayer graphene. *Reports on Progress in Physics*, 76(5):056503, 2013.

[33] K. S. Novoselov, E. McCann, S. V. Morozov, V. I. Fal'ko, M. I. Katsnelson, U. Zeitler, D. Jiang, F. Schedin, and A. K. Geim. Unconventional quantum hall effect and berry's phase of 2π in bilayer graphene. *Nature Physics*, 2(3):177–180, 2006.

[34] E. H. Hwang and S. Das Sarma. Screening, kohn anomaly, friedel oscillation, and rkky interaction in bilayer graphene. *Physical Review Letters*, 101(15):156802, 2008.

[35] J. Nilsson, A. H. Castro Neto, F. Guinea, and N. M. R. Peres. Electronic properties of bilayer and multilayer graphene. *Physical Review B*, 78(4), 2008.

[36] Y.-J. Yu, Y. Zhao, S. Ryu, L. E. Brus, K. S. Kim, and P. Kim. Tuning the graphene work function by electric field effect. *Nano Letters*, 9(10):3430–3434, 2009.

[37] S. Yiğen. *Electronic Thermal Conductivity Measurements in Graphene*. PhD thesis, Concordia University, 2015.

[38] S. Yiğen and A. R. Champagne. Wiedemann-franz relation and thermal-transistor effect in suspended graphene. *Nano Letters*, 14(1):289–93, 2014.

[39] M. S. Dresselhaus, A. Jorio, and R. Saito. Characterizing graphene, graphite, and carbon nanotubes by raman spectroscopy. *Annual Review of Condensed Matter Physics*, 1(1):89–108, 2010.

[40] A. C. Ferrari, J. C. Meyer, V. Scardaci, C. Casiraghi, M. Lazzeri, F. Mauri, S. Piscanec, D. Jiang, K. S. Novoselov, S. Roth, and A. K. Geim. Raman spectrum of graphene and graphene layers. *Physical Review Letters*, 97(18):187401, 2006.

[41] V. Sazonova, Y. Yaish, H. Üstünel, D. Roundy, T. A. Arias, and P. L. McEuen. A tunable carbon nanotube electromechanical oscillator. *Nature*, 431:284, 2004.

[42] M. Will, M. Hamer, M. Muller, A. Noury, P. Weber, A. Bachtold, R. V. Gorbachev, C. Stampfer, and J. Guttinger. High quality factor graphene-based two-dimensional heterostructure mechanical resonator. *Nano Letters*, 17(10):5950–5955, 2017.

[43] S. Deng and V. Berry. Wrinkled, rippled and crumpled graphene: an overview of formation mechanism, electronic properties, and applications. *Materials Today*, 19(4):197–212, 2016.

[44] S. Yiğen, V. Tayari, J. O. Island, J. M. Porter, and A. R. Champagne. Electronic thermal conductivity measurements in intrinsic graphene. *Physical Review B*, 87(24), 2013.

[45] X. Du, I. Skachko, A. Barker, and E. Y. Andrei. Approaching ballistic transport in suspended graphene. *Nature Nanotechnology*, 3:491–495, 2008.

[46] E. Ganz, A. B. Ganz, L.-M. Yang, and M. Dornfeld. The initial stages of melting of graphene between 4000 k and 6000 k. *Physical Chemistry Chemical Physics*, 19(5):3756–3762, 2017.

[47] J. Moser, A. Barreiro, and A. Bachtold. Current-induced cleaning of graphene. *Applied Physics Letters*, 91(16):163513, 2007.

[48] T. Fang, A. Konar, H. L. Xing, and D. Jena. Carrier statistics and quantum capacitance of graphene sheets and ribbons. *Applied Physics Letters*, 91(9), 2007.

[49] V. E. Dorgan, M.-H. Bae, and E. Pop. Mobility and saturation velocity in graphene on sio2. *Applied Physics Letters*, 97(8):082112, 2010.

[50] C. Chen, S. Lee, V. V. Deshpande, G. H. Lee, M. Lekas, K. Shepard, and J. Hone. Graphene mechanical oscillators with tunable frequency. *Nature Nanotechnology*, 8(12):923–7, 2013.

[51] C. Samanta, N. Arora, and A. K. Naik. Tuning of geometric nonlinearity in ultrathin nanoelectromechanical systems. *Applied Physics Letters*, 113(11):113101, 2018.

[52] W. Yi. *Electromechanical Resonators in Grpahene Nanoribbons*. PhD thesis, UC Riverside, 2017.

[53] C. Lee, X. Wei, J. W. Kysar, and J. Hone. Measurement of the elastic properties and intrinsic strength of monolayer graphene. *Science*, 321(5887):385, 2008.

[54] J. U. Lee, D. Yoon, and H. Cheong. Estimation of young's modulus of graphene by raman spectroscopy. *Nano Letters*, 12(9):4444–8, 2012.

[55] J. P. Mathew, A. Bhushan, and M. M. Deshmukh. Tension mediated nonlinear coupling between orthogonal mechanical modes of nanowire resonators. *Solid State Communications*, 282:17–20, 2018.

[56] M.I Katsnelson and A.K Geim. Electron scattering on microscopic corrugations in graphene. *Philosophical Transactions of the Royal Society A*, 366(1863):195–204, 2008.

[57] A. Eichler, J. Moser, J. Chaste, M. Zdrojek, I. Wilson-Rae, and A. Bachtold. Nonlinear damping in mechanical resonators made from carbon nanotubes and graphene. *Nature Nanotechnology*, 6:339, 2011.

[58] V. Sazonova. *A Tunable Carbon Nanotube Resonator*. PhD thesis, Cornell University, 2006.

[59] G. Luo, Z.-Z. Zhang, G.-W. Deng, H.-O. Li, G. Cao, M. Xiao, G.-C. Guo, L. Tian, and G.-P. Guo. Strong indirect coupling between graphene-based mechanical resonators via a phonon cavity. *Nature Communications*, 9(1):383, 2018.

[60] J. C. Flores and L. Palma-Chilla. Dirac fermions duality in graphene: Ripples and fractional dimensions as function of temperature. *Scientific Reports*, 8(1):16250, 2018.